Institutionen för systemteknik
Department of Electrical Engineering

Examensarbete

Target Tracking using Maxwell's Equations

Examensarbete utfört i Reglerteknik
vid Tekniska högskolan i Linköping
av

Niklas Wahlström

LiTH-ISY-EX--10/4373--SE

Linköping 2010

Department of Electrical Engineering
Linköpings universitet
SE-581 83 Linköping, Sweden

Linköpings tekniska högskola
Linköpings universitet
581 83 Linköping

Target Tracking using Maxwell's Equations

Examensarbete utfört i Reglerteknik
vid Tekniska högskolan i Linköping
av

Niklas Wahlström

LiTH-ISY-EX--10/4373--SE

Handledare: **Jonas Callmer**
ISY, Linköpings universitet

Examinator: **Fredrik Gustafsson**
ISY, Linköpings universitet

Linköping, 15 June, 2010

Avdelning, Institution
Division, Department

Division of Automatic Control
Department of Electrical Engineering
Linköpings universitet
SE-581 83 Linköping, Sweden

Datum
Date

2010-06-15

Språk
Language

☐ Svenska/Swedish
☒ Engelska/English

☐ _____

Rapporttyp
Report category

☐ Licentiatavhandling
☒ Examensarbete
☐ C-uppsats
☐ D-uppsats
☐ Övrig rapport
☐ _____

ISBN
—

ISRN
LiTH-ISY-EX--10/4373--SE

Serietitel och serienummer **ISSN**
Title of series, numbering —

URL för elektronisk version
http://www.control.isy.liu.se
http://urn.kb.se/resolve?urn=urn:nbn:se:liu:diva-57693

Titel
Title
Målföljning med Maxwells ekvationer
Target Tracking using Maxwell's Equations

Författare
Author
Niklas Wahlström

Sammanfattning
Abstract

Starting from Maxwell's equations, we derive a sensor model for three-axis magnetometers suitable for localization and tracking applications. The model depends on the relative position between the sensor and the target, orientation of the target and its magnetic signature. Both point targets and extended target models are provided. The models are validated on data taken from various road vehicles. The suitability of magnetometers for tracking is analyzed in terms of local observability and Cramér Rao lower bound as a function of the sensor positions in a two sensor scenario. Also the signal to noise ratio is computed to determine the effective range of the magnetometer. Results from field test data indicate excellent tracking of position and velocity of the target, as well as identification of the magnetic target model suitable for target classification.

Nyckelord
Keywords tracking, magnetic dipole, EKF, filter banks, observability

Abstract

Starting from Maxwell's equations, we derive a sensor model for three-axis magnetometers suitable for localization and tracking applications. The model depends on the relative position between the sensor and the target, orientation of the target and its magnetic signature. Both point targets and extended target models are provided. The models are validated on data taken from various road vehicles. The suitability of magnetometers for tracking is analyzed in terms of local observability and Cramér Rao lower bound as a function of the sensor positions in a two sensor scenario. Also the signal to noise ratio is computed to determine the effective range of the magnetometer. Results from field test data indicate excellent tracking of position and velocity of the target, as well as identification of the magnetic target model suitable for target classification.

Sammanfattning

Utgående från Maxwells ekvationer härleder vi en sensormodel för en tre-axlig magnetometer, lämplig för lokaliserings- och målföljningstillämpningar. Modellen är beroende av den relativa positionen mellan sensorn och målet, målets orientering samt dess magnetiska signatur. Både punktmålsmodeller och utvidgade modeller presenteras. Modellerna valideras med mätningar från varierande fordon. Magnetometrars lämplighet inom målföljning analyseras medelst lokal observerbarhet och Cramér Rao lower bound som en funktion av sensorernas positioner i ett system med två sensorer. Även signal till brus förhållande beräknas för att bestämma den effektiva räckvidden hos en magnetometer. Resultat från fältdata indikerar utmärkt målföljning av position och hastighet för målet, såväl som identifiering av magnetisk signatur som kan användas för målklassifiering.

Acknowledgments

First of all I would like to thank my supervisor Jonas Callmer and my examiner Prof. Fredrik Gustafsson for giving plenty of advices and for being a great support during the thesis work. Your knowledge and ideas have inspired me always taking a step further.

Regarding the experimental data collection a big thanks goes to Daniel Eriksson and David Törnqvist for patiently driving the cars back and forth. The author also wants to thank Nils Jönsson for initiating the project of using magnetometers for tracking, and Prof. Peter Münger for his experts advices on electromagnetism.

Finally, I would thank my family for always believing in what I am doing. Nicky, you deserve my deepest gratitude, every day becomes a little easier when you are here!

Contents

Chapter 1

Introduction

Tracking and classification of targets are primary concerns in automated surveillance systems. The tracking and classification information can be used for statistical purposes, for example counting the number of target of a specific type and registering of their velocities and arrival/heading direction.

Today, the most common method used in traffic flow counting system is *pneumatic road tubes* [8] lying on the surface the road, sensing the pressure of passing vehicles. However, due to extensive physical strain, the equipment will wear approximately within one week [8] at busy roads and can therefore only be used for shorter periods. Furthermore, the technique is only suited for detection and not for estimating vehicle or scenario specific parameters.

Other more sustainable solutions are based on measuring the magnetic properties of the vehicles. We know that ferromagnetic objects induce a magnetic field partly due to the permanently magnetized material in the vehicle and partly due to the deflection of the magnetic field of the earth. Most common sensors sensing metallic objects are *inductive loops*, which is excited with a periodic signal and functions as a inductive element. Presence of metallic objects near the sensor decreases the inductance in the loop which is detected. This extended loop must be buried in the roadway, which results in higher installation costs. Furthermore, like the pneumatic tubes, inductive loops are only suitable for detection.

In this thesis the use of stationary magnetometers for automated surveillance systems will be analyzed. In contrast to the inductive loops, magnetometers passively measures the three-dimensional magnetic field directly and thus contains more information. Furthermore, magnetometers are not dependent of an external wire and can thus be placed beside the road avoiding expensive installation costs.

For moving metallic vehicles, the magnetometer measurements will vary in time, which results in a time dependent signal (see Figure 1.1). This signal depends on the position, speed, orientation (relative to the magnetic field of the earth) and the magnetic signature of the target. This thesis presents nonlinear model-based statistical signal processing methods to be used with this signal in order to track vehicles. Thus, the approach will not be limited to the detection problem, but will also estimate other scenario/target specific parameters. Special interest will be

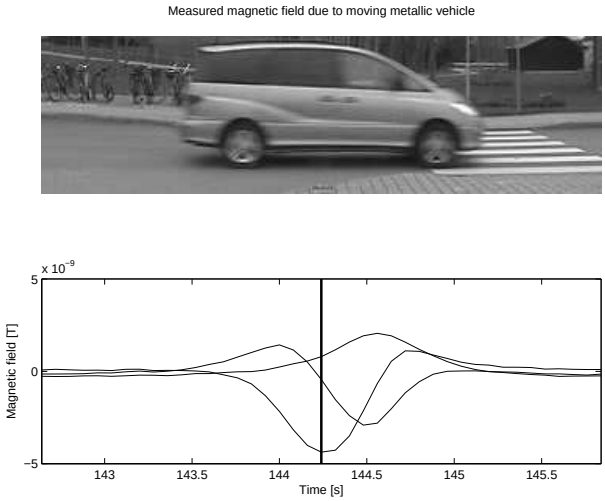

Figure 1.1. A metallic vehicle gives rise to a magnetic field which can be measured with a stationary 3D-magnetometer.

given to the restriction where the vehicles pass the sensor with constant velocity. Moreover, the methods will be evaluated using real experimental data.

The simplest model for the vehicle is to approximate it with a magnetic dipole which is specified with the magnetic dipole moment $\mathbf{m}$. This approximation has been done by many other authors (see Section 1.1). Here some model specific questions arise

- How good is the dipole model?
- How can the dipole model be extended?
- How does $\mathbf{m}$ depend on the vehicle orientation?

Recently, magnetometers have been miniaturized and become cheaper which makes an extensive usage of stationary magnetometer more interesting, not only in automated surveillance systems, but also for tracking, localization and classification of metallic targets in general. Now, more fundamental questions regarding this sensor type arise:

- Is the position, velocity and magnetic signature of the target uniquely identifiable with measurement from one sensor?
- Is there any difference in a two-sensor scenario?
- What is the optimal deployment of the sensors relative the target trajectory?
- What is the effective range of the sensor?

Hence, the thesis will also in more general terms investigate the potential of magnetometers in tracking applications.

1.1 Related work

The most common application of magnetometers is for *navigation*, where the magnetometer mounted to the target measures the stationary magnetic field of the earth. For this purpose, there exists a vast literature.

Our concern is the dual problem - *tracking*, a stationary magnetometer measuring non-stationary magnetic fields due to a moving target. In this field, very little has been done and the following short account will cover the main contributions.

Birsan [1, 2] has used the dipole model for target tracking, where simulations of known positions and magnetic dipole moments have been used to estimate these parameters. Tracking and estimation were performed using an unscented Kalman filter [1] and an unscented particle filter [2]. Furthermore, several studies have been done exploring the use of underwater magnetometers for tracking of vessels [7, 3, 4], where [4] has used the dipole model not only for localizing the vessel, but also for estimating the positions of the sensors. In [3] a Bayesian match-field approach has been used, which takes the attenuation of the seawater into consideration.

In [2], the problem with determining the direction of arrival due to the non-linearity of the sensor model has been addressed, which has been solved with a Monte Carlo based approach known as the particle filter. However, in this work, the vehicle is assumed to follow the roads and only a few number of arrival directions have to been considered, which can be solved by initializing one Extended Kalman Filter for each arrival direction. Furthermore, the works using the dipole model [1, 2, 4] are based on simulations, whereas this work will compare the theory with experimental data. Moreover, this work will analyze possible extended target models to get a better near-field model and for variance estimations of the truncation error. To the best of the author's knowledge, this is the first time it has been done in this context. In addition, the problem with lack of observability for an one-sensor scenario has in [2] been addressed. Our work will more precisely describe this unobservable manifold. Finally, the optimal sensor deployment is analyzed in terms of local observability and Cramér Rao lower bound as a function of the sensor positions in a two-sensor scenario.

The results in Chapter 5, Chapter 6 and 7 have previously been published in [15]. However, [15] is only based on one sensor measurements, whereas this thesis is based on measurements from a two-sensor scenario.

1.2 Thesis Outline

The thesis outline is as follows:

- Chapter 2 presents the relevant estimation and filter theory used in this thesis. Static and dynamic models are describes as well as filter banks.

- Chapter 3 presents the relevant electromagnetic theory in the thesis. Focus will be given to magnetostatics and magnetization.

- Chapter 4 described the state space models of the vehicles and their magnetic signatures.
- Chapter 5 examines the theoretical limitations and possibilities of magnetometers for localization and navigation.
- Chapter 6 validates the state space models with real experimental data for vehicles having constant velocities.
- Chapter 7 illustrates the performance of the models for classification and tracking applications with real experimental data.
- Chapter 8 gives an overall conclusion and directions for future work are discussed.

Chapter 2

Estimation and Filter Theory

All phenomena are governed by some rules, which describe relations between causes and effects. Often these effects can be quantified and measured and the causes can be parameterized. Our aim is to solve this inverse problem, namely to estimate the value of these parameters from the measured data. In this chapter the estimation theory will be introduced, which can be used to solve such inverse problems. Focus will be given to the specific algorithms and techniques that have been used in the thesis. To large extent the presented material is based on theory as it is presented in [10].

Estimation theory is a branch of statistics and signal processing that deals with estimating the values of parameters based on measured data. These parameters describe an underlying setting that affects the distribution of the measured data. In the estimation framework the parameters $\mathbf{x}$ and the measurements $\mathbf{y}$ are regarded as multi-dimensional stochastic variables. Their relation is described with a function $\mathbf{h}$

$$\mathbf{y} = \mathbf{h}(\mathbf{x}, \mathbf{e}), \tag{2.1}$$

where $\mathbf{e}$ also is a stochastic variable known as measurement noise.

The core problem in estimation theory is to find an appropriate function $\mathbf{h}$ with belonging parameters $\mathbf{x}$ and to estimate these parameters. If $\mathbf{h}$ were invertible, the task would be simple, however usually it is not and it has to be approximated by iterative algorithms.

Filter theory can be seen as an extension of the estimation theory in that $\mathbf{x}(t)$ and $\mathbf{e}(t)$ are stochastic processes parameterized with a variable t and $\mathbf{x}(t)$ is governed by a recursive function $\mathbf{f}$

$$\mathbf{x}(t + \Delta t) = \mathbf{f}(\mathbf{x}(t), \mathbf{v}(t)) \tag{2.2}$$

where $\mathbf{v}(t)$ is process noise.

2.1 Discrete State Space Model

In this work the variable t will be interpreted as time and the noise processes $\mathbf{e}(t)$ and $\mathbf{v}(t)$ are assumed to be additive. Furthermore, since computers only can handle discrete data, all stochastic processes are sampled in time at time instances $t_k = kT_s,\ k \in \mathbb{Z}$ where T_s is known as the sample time. Thus, the nonlinear state space model considered here is

$$\mathbf{x}_{k+1} = \mathbf{f}(\mathbf{x}_k) + \mathbf{w}_k \tag{2.3a}$$
$$\mathbf{y}_k = \mathbf{h}(\mathbf{x}_k) + \mathbf{e}_k, \tag{2.3b}$$

where the noise processes $\mathbf{w}_k$ and $\mathbf{e}_k$ are assumed to be independent and identically distributed and drawn from a zero-mean normal distribution with covariance $\mathbf{Q}_k$ and $\mathbf{R}_k$ respectively, i.e.

$$\mathbf{w}_k \sim \mathcal{N}(\mathbf{0}, \mathbf{Q}_k) \tag{2.4a}$$
$$\mathbf{e}_k \sim \mathcal{N}(\mathbf{0}, \mathbf{R}_k). \tag{2.4b}$$

Finally, the measurements $\mathbf{y}_k$ consists of N samples starting at time instance $t_0 = 0$ and ending at $t_{N-1} = (N-1)T_s$.

2.2 Batched System

The process noise $\mathbf{w}_k$ reflects the uncertainty of the evolution of the state. Even if one knows the state $\mathbf{x}_k$ perfectly, one can not predict the state $\mathbf{x}_{k+1}$ with 100% accurancy. However, in some cases the process noise is small and the time horizon N short in comparison to the desired deviation of the estimated state trajectory. In these cases, the process noise can be assumed to be equal to zero $\mathbf{w}_k = 0$ and the state trajectory $\mathbf{x}_{0:N}$ can merely be parametrized by its initial state $\mathbf{x}_0$. All states will be a function of this initial state $\mathbf{x}_{k+1}(\mathbf{x}_0)$ defined by the recursion

$$\mathbf{x}_{k+1} = \mathbf{f}(\mathbf{x}_k). \tag{2.5}$$

By defining

$$\mathbf{h}_k(\mathbf{x}_0) = \mathbf{h}(\mathbf{x}_k(\mathbf{x}_0)), \tag{2.6}$$

the system (2.3) can be described in batch formulation

$$\mathbf{y}_k = \mathbf{h}_k(\mathbf{x}_0) + \mathbf{e}_k, \quad k = 1 \dots N. \tag{2.7}$$

2.3 Nonlinear Weighted Least Squares Estimation

The nonlinear weighted least squares estimate (NWLS) for the model (2.7) is defined as the solution to the optimization problem

$$\hat{\mathbf{x}} = \arg\min_{\mathbf{x}} V^{NWLS}(\mathbf{x}) \tag{2.8a}$$

$$V^{NWLS}(\mathbf{x}) = \sum_{k=1}^{N} (\mathbf{y}_k - \mathbf{h}_k(\mathbf{x}))^T \mathbf{R}_k^{-1} (\mathbf{y}_k - \mathbf{h}_k(\mathbf{x})). \tag{2.8b}$$

Since the optimization problem is nonlinear, an iterative process has to be applied for solving it. There are many algorithms available for minimizing such functions and most of them are based on a linearization of (2.7) at each iteration point $\mathbf{x}^{(i)}$

$$\mathbf{y}_k \approx \mathbf{h}_k(\mathbf{x}^{(i)}) + \boldsymbol{\nabla}\mathbf{h}_k(\mathbf{x}^{(i)})\mathbf{x}^{(i)} + \mathbf{e}_k \Rightarrow \tag{2.9a}$$

$$\bar{\mathbf{y}}_k = \mathbf{H}_k \mathbf{x}^{(i)} + \mathbf{e}_k, \tag{2.9b}$$

where $\mathbf{H}_k = \boldsymbol{\nabla}\mathbf{h}_k(\mathbf{x}^{(i)})$ and $\bar{\mathbf{y}}_k = \mathbf{y}_k - \mathbf{h}_k(\mathbf{x}^{(i)})$. The most basic of these algorithms is the *Method of Gradient Descent*, where the line search is defined as the negative gradient of the cost function (2.8b)

$$\mathbf{s}^{(i)} = -\boldsymbol{\nabla} V(\mathbf{x}^{(i)}) = 2 \sum_{k=1}^{N} \mathbf{H}_k^T \mathbf{R}_k^{-1} \bar{\mathbf{y}}_k. \tag{2.10}$$

Another algorithm is the *Gauss-Newton algorithm* (GN), where the line search is found by solving the linear weighted least square problem.

$$\left(\sum_{k=1}^{N} \mathbf{H}_k^T \mathbf{R}_k^{-1} \mathbf{H}_k \right) \mathbf{s}^{(i)} = \sum_{k=1}^{N} \mathbf{H}_k^T \mathbf{R}_k^{-1} \bar{\mathbf{y}}_k \tag{2.11}$$

The *Levenberg-Marquardt algorithm* (LM) combines these algorithms by adding a scalar multiple of the identity matrix in the weighted least square equations.

$$\left(\mu \mathbf{I} + \sum_{k=1}^{N} \mathbf{H}_k^T \mathbf{R}_k^{-1} \mathbf{H}_k \right) \mathbf{s}^{(i)} = \sum_{k=1}^{N} \mathbf{H}_k^T \mathbf{R}_k^{-1} \bar{\mathbf{y}}_k \tag{2.12}$$

This correction will help if the problem is ill-conditioned or rank-deficient, which often is the case in problems in this thesis. The (non-negative) damping factor μ is adjusted at each iteration. If reduction of the cost function V is rapid, a smaller value can be used, bringing the algorithm closer to the GN, whereas if an iteration gives insufficient reduction in the residual, μ is increased, giving a step closer to the gradient descent direction. The procedure is described in Algorithm 1.

At optimum we have $\boldsymbol{\nabla} V(\hat{\mathbf{x}}) = \mathbf{0}$ and

Algorithm 1 Levenberg-Marquardt Algorithm

1. Given initial value $\hat{\mathbf{x}}^{(0)}$. Set $i = 0$ and choose a $\mu > 0$.
2. Compute $\mathbf{H}_k = \boldsymbol{\nabla}\mathbf{h}_k(\mathbf{x}^{(i)})$ and $\bar{\mathbf{y}}_k = \mathbf{y}_k - \mathbf{h}_k(\mathbf{x}^{(i)})$ for all $k = 1 \dots N$
3. Solve $\left(\mu\mathbf{I} + \sum_{k=1}^{N} \mathbf{H}_k^T \mathbf{R}_k^{-1} \mathbf{H}_k\right) \mathbf{s}^{(i)} = \sum_{k=1}^{N} \mathbf{H}_k^T \mathbf{R}_k^{-1} \bar{\mathbf{y}}_k$
4. Set $\mathbf{x}^{(i+1)} := \mathbf{x}^{(i)} + \mathbf{s}^{(i)}$
5. If the cost $V(\hat{\mathbf{x}}^{(i+1)}) > V(\hat{\mathbf{x}}^{(i)})$ has increased, set $\mu := 2\mu$ and repeat from step 2.
6. Terminate if the change in cost, the change in estimate, or the size of the gradient is small enough.
7. Otherwise, set $\mu = \mu/2$, $i := i + 1$ and repeat from step 2.

$$\mathbf{0} = \boldsymbol{\nabla} V(\hat{\mathbf{x}}) \approx 2 \sum_{k=1}^{N} \mathbf{H}_k^T \mathbf{R}_k^{-1} (\mathbf{H}_k \hat{\mathbf{x}} + \mathbf{e}_k) \Rightarrow \tag{2.13a}$$

$$\hat{\mathbf{x}} \approx \left(\sum_{k=1}^{N} \mathbf{H}_k^T \mathbf{R}_k^{-1} \mathbf{H}_k \right)^{-1} \sum_{k=1}^{N} \mathbf{H}_k^T \mathbf{R}_k^{-1} \mathbf{e}_k \Rightarrow \tag{2.13b}$$

$$\mathrm{Cov}(\hat{\mathbf{x}}) \approx \left(\sum_{k=1}^{N} \mathbf{H}_k^T \mathbf{R}_k^{-1} \mathbf{H}_k \right)^{-1} = \left(\sum_{k=1}^{N} \boldsymbol{\nabla}\mathbf{h}_k(\hat{\mathbf{x}})^T \mathbf{R}_k^{-1} \boldsymbol{\nabla}\mathbf{h}_k(\hat{\mathbf{x}}) \right)^{-1}, \tag{2.13c}$$

which provides a measure of how good the estimate is.

2.4 Cramér Rao Lower Bound

The approximation of the covariance matrix in (2.13c) is parameterized with the estimate $\hat{\mathbf{x}}$ of the true parameter $\mathbf{x}^0$. For this reason, only an approximation of the covariance can be provided. The question is, how good is this approximation? The answer is partly given by the *Cramér Rao lower bound* (CRLB), which provides a theoretical lower bound of the covariance matrix, which briefly will be presented in this section. More details can be found in [10].

The *Fisher Information matrix* (FIM) for one measurement $\mathbf{y}_k$ is defined as

$$\mathcal{I}_k(\mathbf{x}^0) = E\left[\left(\frac{d \log p(\mathbf{y}_k | \mathbf{x}^0)}{d\mathbf{x}^0} \right) \left(\frac{d \log p(\mathbf{y}_k | \mathbf{x}^0)}{d\mathbf{x}^0} \right)^T \right] \tag{2.14}$$

For the model (2.7), the FIM is shown to be

$$\mathcal{I}_k(\mathbf{x}^0) = \boldsymbol{\nabla}\mathbf{h}_k^T(\mathbf{x}^0) \mathbf{R}_k^{-1} \boldsymbol{\nabla}\mathbf{h}_k(\mathbf{x}^0), \tag{2.15}$$

Since information is additive for independent observations, we have

$$\mathcal{I}_{1:N}(\mathbf{x}^0) = \sum_{k=1}^{N} \nabla \mathbf{h}_k^T(\mathbf{x}^0) \mathbf{R}_k^{-1} \nabla \mathbf{h}_k(\mathbf{x}^0), \tag{2.16}$$

Now, the CRLB states that for any unbiased estimator $\hat{\mathbf{x}}$, the following inequality must hold

$$\text{Cov}(\hat{\mathbf{x}}) \geq \mathcal{I}_{1:N}(\mathbf{x}^0)^{-1} \tag{2.17}$$

Thus, CRLB provides a lower theoretical bound of the covariance matrix. Note, that $\mathcal{I}_{1:N}$ has to be parameterized with the true parameter $\mathbf{x}^0$. The theorem, can therefore only be applied if $\mathbf{x}^0$ is known, i.e. for simulations or for real measurements done together with ground truth reference data.

2.5 Extended Kalman Filter

If the assumption in Section 2.2 that the process noise $\mathbf{w}_k$ is negligible does not hold, the whole nonlinear system (2.3) has to be considered. Due to this nondeterministic feature a recursive algorithm has to be applied. In the linear case, the famous *Kalman Filter* is the *Best Linear Unbiased Estimator* (BLUE). In the nonlinear case, the equivalent algorithm is the *Extended Kalman Filter* (EKF), which basically is an implementation of the Kalman Filter for the linearized version of (2.3). The EKF is presented in Algorithm 2.

Note that the EKF is only BLUE for the linearized version of the nonlinear model and not for the nonlinear model itself. Thus, in order to make the EKF perform well, the linearization has to be a good approximation of the nonlinear model. A good linearization is normally achieved by linearizing close to the the true state $\mathbf{x}_k^0$. However, the true state is not known, only an estimate $\hat{\mathbf{x}}_{k|k-1}$ of it is available. Therefore, in order to make the EKF to perform well, the distance $||\mathbf{x}_k^0 - \hat{\mathbf{x}}_{k|k-1}||$ has to be small. Thus, a good initial guess $\hat{\mathbf{x}}_0$ can be crucial.

2.6 Filter Banks for Multi Hypotheses Testing

In the EKF an initial guess of the state has to be provided, which has to be based on some prior knowledge of the state at time $t = 0$. In Section 2.5 we have seen that a good initial guess can be crucial for the EKF to perform well.

If the prior knowledge of the state is based on different hypotheses, whose state guesses are well-separated in the state space, one EKF for each hypothesis must be initialized in order to make it plausible that the one corresponding to the correct hypothesis converge to the optimal solution. Note that no optimality is guaranteed, we only maximize the probability to find a solution close to the optimal solution. To evaluate the correctness of the different hypotheses, the Filter Bank theory can be addressed. In this framework the model (2.3) can be slightly extended to include a discrete parameter δ. Here $\delta \in M$ represents the different hypotheses.

Algorithm 2 Extended Kalman Filter

Given initial state $\hat{\mathbf{x}}_{1|0}$, and initial error covariance $\mathbf{P}_{1|0}$

1. Perform linearization by computing

$$\mathbf{H}_k = \boldsymbol{\nabla}\mathbf{h}(\hat{\mathbf{x}}_{k|k-1}) \tag{2.18a}$$
$$\mathbf{F}_k = \boldsymbol{\nabla}\mathbf{f}(\hat{\mathbf{x}}_{k|k-1}) \tag{2.18b}$$

2. Perform measurement update by computing

$$\hat{\mathbf{y}}_{k|k-1} = \mathbf{h}(\hat{\mathbf{x}}_{k|k-1}) \tag{2.19a}$$
$$\mathbf{S}_{k|k-1} = \mathbf{H}_k\mathbf{P}_{k|k-1}\mathbf{H}_k^T + \mathbf{R}_k \tag{2.19b}$$
$$\mathbf{K}_k = \mathbf{P}_{k|k-1}\mathbf{H}_k^T\mathbf{S}_{k|k-1}^{-1} \tag{2.19c}$$
$$\hat{\mathbf{x}}_{k|k} = \hat{\mathbf{x}}_{k|k-1} + \mathbf{K}_k(\mathbf{y}_k - \hat{\mathbf{y}}_{k|k-1})) \tag{2.19d}$$
$$\mathbf{P}_{k|k} = (\mathbf{I} - \mathbf{K}_k\mathbf{H}_k)\mathbf{P}_{k|k-1} \tag{2.19e}$$

3. Perform time update by computing

$$\hat{\mathbf{x}}_{k+1|k} = \mathbf{f}(\hat{\mathbf{x}}_{k|k}) \tag{2.20a}$$
$$\mathbf{P}_{k+1|k} = \mathbf{F}_k\mathbf{P}_{k|k}\mathbf{F}_k^T + \mathbf{Q}_k \tag{2.20b}$$

The model is now defined by

$$\mathbf{x}_{k+1} = \mathbf{f}(\mathbf{x}_k, \delta) + \mathbf{v}_k(\delta) \tag{2.21a}$$
$$\mathbf{y}_k = \mathbf{h}(\mathbf{x}_k, \delta) + \mathbf{e}_k(\delta) \tag{2.21b}$$
$$\mathbf{x}_0 \sim \mathcal{N}(\hat{\mathbf{x}}_0(\delta), \mathbf{P}(\delta)) \tag{2.21c}$$
$$\delta \in M. \tag{2.21d}$$

According to (2.21), even the model components $\mathbf{f}$, $\mathbf{h}$, $\mathbf{v}_k$ and $\mathbf{e}_k$ can be parameterized with δ. However, in our setup the hypotheses only differ in its initial guesses $\mathbf{x}_0 \sim \mathcal{N}(\hat{\mathbf{x}}_0(\delta), \mathbf{P}(\delta))$.

Furthermore, this concept can be extended by interpreting the parameter δ_k as the mode of the system at time instance k and allowing transitions. This will result in a jump Markov model suitable for change detection. However, this will not be considered here, see [10] for further details.

At each iteration *a postiori* probabilities of each model will be computed as

$$w_k^\delta = p(\delta|\mathbf{y}_{1:k}) = \frac{p(\delta)}{p(\mathbf{y}_{1:k})} p(\mathbf{y}_{1:k}|\delta) \tag{2.22a}$$

$$= \frac{p(\delta)}{p(\mathbf{y}_k|\mathbf{y}_{1:k-1})p(\mathbf{y}_{1:k-1})} p(\mathbf{y}_k|\delta, \mathbf{y}_{1:k-1}) p(\mathbf{y}_{1:k-1}|\delta) \tag{2.22b}$$

$$= w_{k-1}^\delta \frac{p(\mathbf{y}_k|\delta, \mathbf{y}_{1:k-1})}{p(\mathbf{y}_k|\mathbf{y}_{1:k-1})}. \tag{2.22c}$$

The EKF provides the measurement prediction $\hat{\mathbf{y}}_{k|k-1}(\delta)$ (see (2.19a)) and its associated covariance $\mathbf{S}_{k|k-1}(\delta)$ (see (2.19b)). The unnormalized model weights can therefore be updated according to

$$w_k^\delta \propto w_{k-1}^\delta \mathcal{N}(\mathbf{y}_k; \hat{\mathbf{y}}_{k|k-1}(\delta), \mathbf{S}_{k|k-1}(\delta)), \tag{2.23}$$

where $\mathcal{N}(\mathbf{y}; \mathbf{m}, \mathbf{P})$ is the evaluation of the probability density function of $\mathcal{N}(\mathbf{m}, \mathbf{P})$ at $\mathbf{y}$. After normalizing, one of the weights w_k^δ will converge to 1 and all other to 0 indicating the correct hypothesis. The sequential computation of the weight can help us to sequentially exclude the incorrect hypotheses, see Algorithm 3. Normally, in the Filter Bank approach where mode transitions are allowed, the different modes δ_k are merged at each step in order o avoid the exponential growing of the number of sequences $\delta_{1:k}$ (as before, see [10] for more details). However, since no mode transitions are allowed in this case, the merging step is not needed. In fact, merging the correct hypotheses with the incorrect hypotheses produce an estimate that does not make any sense at all.

Algorithm 3 Filter Bank for Multi Hypotheses Test

Initialize the weights $w_0^\delta = 1/|M|$ for $\delta \in M$, set $M_0 = M$ and choose a threshold τ.

1. Perform measurement and time update for all $\delta \in M_{k-1}$ (see Algorithm 2)
2. Weight measurement update for $\delta \in M_{k-1}$

$$\bar{w}_k^\delta = w_{k-1}^\delta \mathcal{N}(\mathbf{y}_k; \hat{\mathbf{y}}_{k|k-1}(\delta), \mathbf{S}_{k|k-1}(\delta)) \tag{2.24a}$$

$$w_k^\delta = \frac{\bar{w}_k^\delta}{\sum_{\delta' \in M_{k-1}} \bar{w}_k^{\delta'}} \tag{2.24b}$$

3. Keep the most likely hypotheses $M_k = \{\delta \in M_{k-1} | w_k^\delta > \tau\}$ and repeat from step 1.

Chapter 3

Electromagnetic Theory

In Chapter 2 the estimation and filter theory was introduced. All presented methods and algorithms were based on a mathematical model (2.3) of the observed phenomena. However, not a word was given to what this model should look like. To be able to derive such a model, the relevant theory has to be addressed. In this thesis, that theory will be the electromagnetic theory. In this chapter, we will introduce the electromagnetic theory in general and more specifically deal with magnetostacis, which of special interest for this thesis.

Even though electromagnetic phenomena were known to the ancient Greeks, it started its development as a quantitative subject first in the end of the 18th century with Cavendish' and Columbus' experiments and research. Fifty years later Faraday was studying time varying electromagnetic phenomena. By 1865 James Clerk Maxwell had published his famous paper on a dynamical theory of the electromagnetic field [13]. In this paper the original set of four Maxwell's equations first appeared. These equations will be our theoretical starting point.

3.1 Maxwell's Equations

All electromagnetic phenomena are governed by Maxwell's equations which are

$$\boldsymbol{\nabla} \cdot \mathbf{E} = \frac{\rho}{\varepsilon_0} \tag{3.1a}$$

$$\boldsymbol{\nabla} \times \mathbf{B} - \mu_0 \varepsilon_0 \frac{\partial \mathbf{E}}{\partial t} = \mu_0 \mathbf{J} \tag{3.1b}$$

$$\boldsymbol{\nabla} \times \mathbf{E} + \frac{\partial \mathbf{B}}{\partial t} = \mathbf{0} \tag{3.1c}$$

$$\boldsymbol{\nabla} \cdot \mathbf{B} = 0, \tag{3.1d}$$

where $\mathbf{E}$ is the electric field, ρ is the charge density, $\mathbf{B}$ is the magnetic field and $\mathbf{J}$ is the current density. (3.1) are given in SI units. Apart from the fields $\mathbf{E}$ and $\mathbf{B}$ and its sources ρ and $\mathbf{J}$ the equations also include the constants ε_0 and μ_0. ε_0 andμ_0 are the permittivity and permeability of free space respectively. The permeability

of free space μ_0 has an exactly defined value

$$\mu_0 = 4\pi 10^{-7} = 1.257 \cdot 10^{-6} \text{ [F/m]}, \tag{3.2}$$

and the permittivity of free space is defined by

$$\varepsilon_0 = 1/(\mu_0 c_0^2) = 8.854 \cdot 10^{-12} \text{ [H/m]}, \tag{3.3}$$

where c_0 is the speed of light. Table 3.1 summarizes the meaning of each symbol and the SI unit of measure.

Table 3.1. Definitions and units.

Symbol	Meaning	SI unit
$\mathbf{E}$	Electric field	Volt per meter [V/m]
$\mathbf{B}$	Magnetic field	Tesla [T]
ρ	Charge density	Coulombs per cubic meter [C/m^3]
$\mathbf{J}$	Current density	Amperes per square meter [A/m^2]
ε_0	Permittivity of free space	Farads per meter [F/m]
μ_0	Permeability of free space	Henries per meter [H/m]

3.2 Quasi-static approximation

In this thesis, the magnetic field $\mathbf{B}$ is of special interest, since that is the quantity that will be measured. In general, it is coupled with the electric field $\mathbf{E}$ through their time derivatives (3.1b) and (3.1c). However, in the stationary case the terms $\partial\mathbf{E}/\partial t$ and $\partial\mathbf{B}/\partial t$ can be neglected, and Maxwell's equations will be decoupled. The magnetic field will therefore obey the magnetostatic equations

$$\boldsymbol{\nabla} \times \mathbf{B} = \mu_0 \mathbf{J} \tag{3.4a}$$

$$\boldsymbol{\nabla} \cdot \mathbf{B} = 0. \tag{3.4b}$$

Form these equations it is clear that the current density $\mathbf{J}$ can be regarded as the source causing the magnetic filed $\mathbf{B}$. If the current density is time-dependent, the static assumption does not hold and the full solution of Maxwell's equations has to be considered. However, if these changes are sufficiently small, a *quasi-static approximation* can be made, in which the magnetostatic equations (3.4) still hold. In this approximation, (3.4a) states that any variation in the current density $\mathbf{J}$ is instantaneously communicated to the magnetic field $\mathbf{B}$, showing that the velocity of propagation is infinite. Hence, this approximation is only valid if the time lag produced by the finite velocity of propagation is very small in comparison with the time interval in which the currents undergo relevant changes. If the changes are periodical with a certain frequency the condition of quasi-stationarity can be expressed as

$$\text{size of the physical system} \times \text{frequency} \ll c_0 = \text{speed of light} \tag{3.5}$$

Example 3.1

For a transformer with the characteristic size ~ 30 cm and a frequency of 50 Hz we have

$$\text{size} \times \text{frequency} = 30 \text{ cm} \times 50\text{s}^{-1} = 1500 \text{ m/s} \ll c_0$$

Thus, in a transformer the quasi-static approximation is valid.

3.3 Magnetic dipole

According to Maxwell's equations (3.1), a current density $\mathbf{J}$ will induce a magnetic field $\mathbf{B}$. In section 3.2, we have seen that this dependency can be simplified to (3.4) if a static or quasi-static case is considered. In this section, we will compute this induced magnetic $\mathbf{B}$ field due to a localized current density.

Consider a region with localized current density. That means, charged particles can move within the region, but neither leave it nor be added to it. According to (3.4), this current density gives rise to an induced magnetic field outside the region (see Figure 3.1). Since $\boldsymbol{\nabla} \cdot \mathbf{B} = 0$ everywhere, $\mathbf{B}$ must be the curl of some

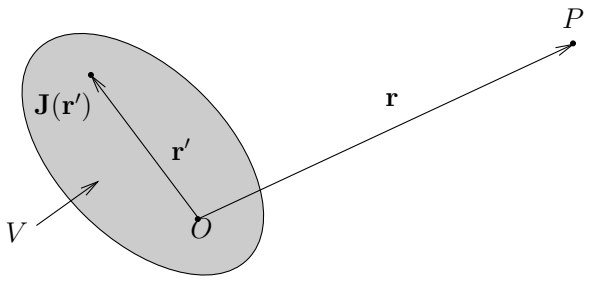

Figure 3.1. Localized current density $\mathbf{J}(\mathbf{r}')$ gives rise to a magnetic induction at the point P with coordinate $\mathbf{r}$.

vector field $\mathbf{A}(\mathbf{r})$, called the *vector potential*

$$\mathbf{B}(\mathbf{r}) = \boldsymbol{\nabla} \times \mathbf{A}(\mathbf{r}). \tag{3.6}$$

Substituting (3.6) into (3.4a) gives

$$\boldsymbol{\nabla} \times (\boldsymbol{\nabla} \times \mathbf{A}(\mathbf{r})) = \mu_0 \mathbf{J} \quad \Rightarrow \tag{3.7a}$$

$$\boldsymbol{\nabla}(\boldsymbol{\nabla} \cdot \mathbf{A}(\mathbf{r})) - \nabla^2 \mathbf{A}(\mathbf{r}) = \mu_0 \mathbf{J}. \tag{3.7b}$$

Since (3.6) only specifies the curl of $\mathbf{A}$, the freedom of the so called gauge transformation allows one to make $\boldsymbol{\nabla} \cdot \mathbf{A}$ have any convenient functional. With

the choice $\boldsymbol{\nabla} \cdot \mathbf{A} = 0$. Each rectangular component of the vector potential satisfies the Poisson's equation

$$\nabla^2 \mathbf{A} = -\mu_0 \mathbf{J}, \tag{3.8}$$

which has the solution

$$\mathbf{A}(\mathbf{r}) = \frac{\mu_0}{4\pi} \int \frac{\mathbf{J}(\mathbf{r}')}{|\mathbf{r} - \mathbf{r}'|} d^3\mathbf{r}'. \tag{3.9}$$

Since $\mathbf{J}(\mathbf{r}') \neq 0$ only in the region of the localized current density V, we have

$$\mathbf{A}(\mathbf{r}) = \frac{\mu_0}{4\pi} \int_V \frac{\mathbf{J}(\mathbf{r}')}{|\mathbf{r} - \mathbf{r}'|} d^3\mathbf{r}'. \tag{3.10}$$

Furthermore, the denominator in (3.10) can be expanded in powers of $\mathbf{r}'$. With $r > r'$ this will be

$$\begin{aligned} \frac{1}{|\mathbf{r} - \mathbf{r}'|} = \frac{1}{r} + (-\mathbf{r}')^T \boldsymbol{\nabla} \left(\frac{1}{r}\right) + \\ \frac{1}{2!} (-\mathbf{r}')^T \left(\boldsymbol{\nabla}\boldsymbol{\nabla} \left(\frac{1}{r}\right)\right) (-\mathbf{r}') + \ldots, \end{aligned} \tag{3.11}$$

where $r = |\mathbf{r}|$. By using this Taylor expansion in (3.9) one gets

$$A_i(\mathbf{r}) = \frac{\mu_0}{4\pi} \left(\frac{1}{r} \int_V J_i(\mathbf{r}') d^3\mathbf{r}' + \frac{\mathbf{r}}{r^3} \cdot \int_V J_i(\mathbf{r}') \mathbf{r}' d^3\mathbf{r}' + \ldots \right). \tag{3.12}$$

Due to the fact that the current density $\mathbf{J}(\mathbf{r})$ is localized and obeys the static continuity condition $\boldsymbol{\nabla} \cdot \mathbf{J} = 0$, Gauss' theorem makes the first term in (3.12) zero. Furthermore, it can be shown that

$$\mathbf{r} \cdot \int_V \mathbf{r}' J_i d^3\mathbf{r}' = (\mathbf{m} \times \mathbf{r})_i, \tag{3.13}$$

where $\mathbf{m}$ is the *magnetic dipole moment*

$$\mathbf{m} = \frac{1}{2} \int_V \mathbf{r}' \times \mathbf{J}(\mathbf{r}') d^3\mathbf{r}'. \tag{3.14}$$

The details of these steps are clearly outlined in [12]. By truncating (3.12) and using (3.14) in (3.12), we get

$$\mathbf{A}(\mathbf{r}) = \frac{\mu_0}{4\pi} \frac{\mathbf{m} \times \mathbf{r}}{r^3}. \tag{3.15}$$

The induced magnetic field can be calculated directly by evaluating the curl of (3.15).

$$\mathbf{B}(\mathbf{r}) = \frac{\mu_0}{4\pi}\frac{3(\mathbf{r}\cdot\mathbf{m})\mathbf{r} - r^2\mathbf{m}}{r^5} \tag{3.16}$$

When $r \gg r'$ the truncation of the Taylor expansion in (3.11) makes a good approximation, i.e. if the characteristic length of region V is small in comparison to the distance from the region to the observer at point P

3.4 Magnetization

In Section 3.3 we have seen that each region of localized current has a uniquely defined magnetic dipole moment. If we assume that the current density can be localized to even smaller regions, we could divide this region into sub-regions and for each of them compute its magnetic dipole moment by using (3.14) and integrate over each sub-region

$$\mathbf{m}_i = \frac{1}{2}\int_{V_i} \mathbf{r}' \times \mathbf{J}(\mathbf{r}')d^3\mathbf{r}'. \tag{3.17}$$

The magnetic dipole moment of the whole region is then the sum of the magnetic dipole moment of each sub-region, since

$$\mathbf{m}_{tot} = \frac{1}{2}\int_{V} \mathbf{r}' \times \mathbf{J}(\mathbf{r}')d^3\mathbf{r}' = \sum_i \frac{1}{2}\int_{V_i} \mathbf{r}' \times \mathbf{J}(\mathbf{r}')d^3\mathbf{r}' = \sum_i \mathbf{m}_i. \tag{3.18}$$

Thus, the superposition is valid for magnetic dipole moments. This is also illustrated in Figure 3.2.

Ferromagnetic material (iron, steel, etc.) can be regarded to consist of such subregions. Normally the magnetic dipole moment of a sub-region is independent of all other subregions making the total dipole moment of that piece of material zero. However, with application of an external magnetic field, an alignment of the internal dipole moments will take place. This alignment property is specific to each ferromagnetic material and to the applied external magnetic field. In order to define this coupling, new physical quantities have to be defined.

Let $\mathbf{m}_i$ be the magnetic dipole moment of an atom. If there are n atoms per unit volume, we define the *magnetization* or the magnetic moment density

$$\mathbf{M} = \lim_{\Delta v \to 0} \frac{\sum_{i=1}^{n\Delta v} \mathbf{m}_i}{\Delta v} \quad [\mathrm{A/m}]. \tag{3.19}$$

where $\sum_{i=1}^{n\Delta v} \mathbf{m}_i$ is summarizing over all magnetic dipole moments within the volume element Δv.

The magnetization $\mathbf{M}$ makes a contribution to the current density $\mathbf{J}$, known as the *magnetization current* $\mathbf{J}_m$ or bound current. By using (3.9), (3.14), (3.15) and (3.19) (calculations outlined in [12, 6]) this current is the curl of the magnetization

$$\boldsymbol{\nabla} \times \mathbf{M} = \mathbf{J}_m \quad [\mathrm{A/m^2}]. \tag{3.20}$$

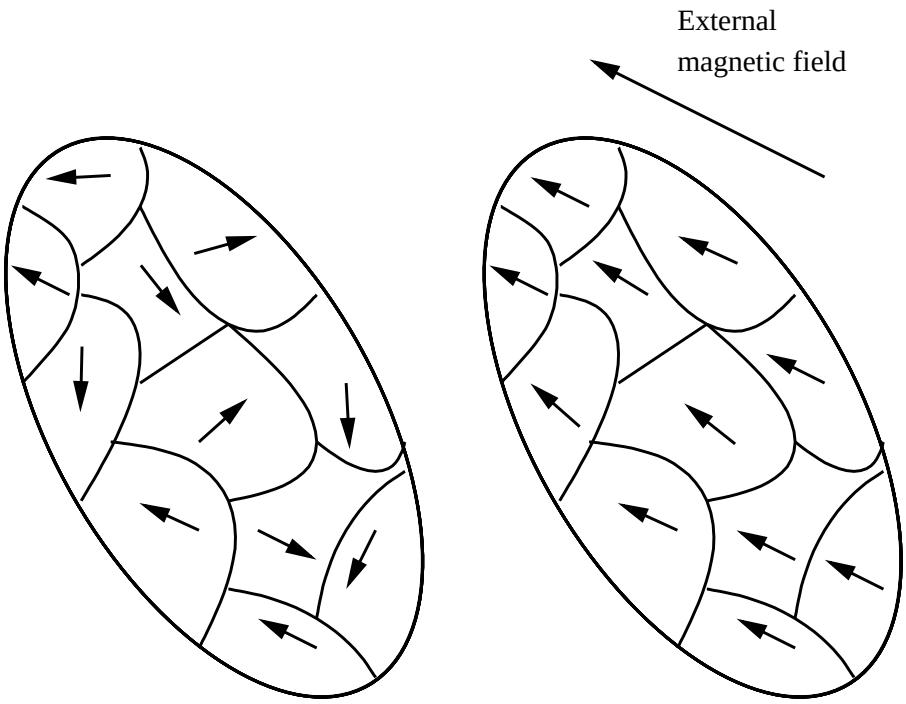

(a) Non-magnetized material. All dipoles are independent of each other and thus $\mathbf{m}_{tot} = \sum \mathbf{m}_i \approx \mathbf{0}$

(b) Magnetized material. The dipoles are aligned in the applied external magnetic filed and therefore $\mathbf{m}_{tot} = \sum \mathbf{m}_i \neq \mathbf{0}$

Figure 3.2.

The total current density can be divided into magnetization current $\mathbf{J}_m$ that is bounded to each atom (i.e. orbiting electrons) and *free current* $\mathbf{J}_f$ that is not bounded to a single atom (currents in electric cables etc)

$$\mathbf{J} = \mathbf{J}_f + \mathbf{J}_m. \tag{3.21}$$

By introducing this division in (3.4a) we get

$$\frac{1}{\mu_0}\boldsymbol{\nabla} \times \mathbf{B} = \mathbf{J}_f + \mathbf{J}_m = \mathbf{J}_f + \boldsymbol{\nabla} \times \mathbf{M} \tag{3.22}$$

or

$$\boldsymbol{\nabla} \times \left(\frac{\mathbf{B}}{\mu_0} - \mathbf{M} \right) = \mathbf{J}_f. \tag{3.23}$$

Now, a new field $\mathbf{H}$ can be defined called the *magnetizing field*

$$\mathbf{H} = \frac{\mathbf{B}}{\mu_0} - \mathbf{M} \quad [\mathrm{A/m}]. \tag{3.24}$$

With this quantity, an alternative version of the magnetostatic equation only including the free current can be given as

$$\boldsymbol{\nabla} \times \mathbf{H} = \mathbf{J}_f \tag{3.25}$$

$$\boldsymbol{\nabla} \cdot \mathbf{B} = \mathbf{0}. \tag{3.26}$$

To complete this description of the magnetostatics, there must be a material specific relation between $\mathbf{H}$ and $\mathbf{B}$. If the magnetic properties of the material are linear and isotropic there is a linear relation

$$\mathbf{B} = \mu \mathbf{H}, \tag{3.27}$$

where μ is a material specific constant called the *magnetic permeability*. For vacuum $\mu = \mu_0$ and for ferromagnetic material $\mu \gg \mu_0$. For convenience, we also talk about *relative permeability* $\mu_r = \frac{\mu}{\mu_0}$. For vacuum $\mu_r = 1$ and for a ferromagnetic substance $\mu_r \gg 1$.

The constitutive relation (3.27) is a relation between the $\mathbf{B}$- and $\mathbf{H}$-field inside the material. An interesting question is how the magnetic field in the material $\mathbf{B}_{in}$ is related to the applied external field $\mathbf{B}_0$. This is far from trivial, and can analytically only be solved for very symmetric objects. For a sphere (see Figure 3.3a), [12] has shown that

$$\mathbf{B}_{in} + \frac{2}{\mu_0}\mathbf{H}_{in} = 3\mathbf{B}_0 \Rightarrow \tag{3.28}$$

$$\mathbf{B}_{in} + \frac{2}{\mu_r}\mathbf{B}_{in} = 3\mathbf{B}_0 \Rightarrow \tag{3.29}$$

$$\mathbf{B}_{in} = \frac{3\mu_r}{\mu_r + 2}\mathbf{B}_0 \Rightarrow \tag{3.30}$$

$$\mathbf{H}_{in} = \frac{1}{\mu_0}\frac{3}{\mu_r + 2}\mathbf{B}_0. \tag{3.31}$$

With (3.24) we get,

$$\mathbf{M} = \frac{\mathbf{B}_{in}}{\mu_0} - \mathbf{H}_{in} = \frac{3}{\mu_0}\frac{\mu_r - 1}{\mu_r + 2}\mathbf{B}_0. \tag{3.32}$$

Now, we can find a relation between the magnetic dipole moment and the volume V of the sphere

$$\mathbf{m} = \int_V \mathbf{M} dv = \frac{3V}{\mu_0}\frac{\mu_r - 1}{\mu_r + 2}\mathbf{B}_0. \tag{3.33}$$

Since $\mu_r \gg 1$ it can be approximated

$$\mathbf{m} \approx \frac{3V}{\mu_0}\mathbf{B}_0. \tag{3.34}$$

[12] has also shown that with the assumption $\mu_r \gg 1$, the induced magnetic moment of a spherical shell will only depend on its outer radius and not on its inner radius (see Figure 3.3), i.e. (3.34) will also hold for spherical shells. This can be used in the following intellectual experiment.

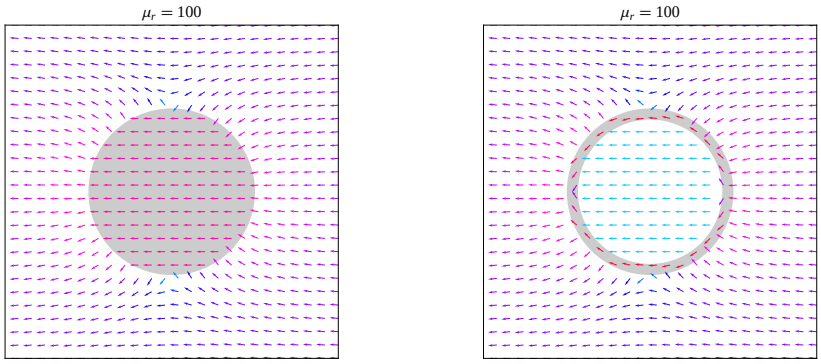

(a) A permeable sphere in a homogeneous magnetic filed.

(b) A magnetized spherical shell.

Figure 3.3. A permeable sphere and a spherical shell in a homogeneous magnetic field $\mathbf{B}_0$. The gray region has $\mu_r = 100$ and the white region $\mu_r = 1$. They both produce equally large induced magnetic fields (see the vector field outside the two regions). Only the outer radius and not the inner radius defines the induced magnetic dipole moment if $\mu_r \gg 1$.

Example 3.2

Consider a non permeable spherical object with volume V and $\mu_r = 1$ which contains ferromagnetic material of total volume V_{fer} and with $\mu_r \gg 1$ (see Figure 3.4). How does the induced magnetic dipole moment depend on the spatially distribution of V_{fer} inside V? By assuming that V_{fer} constitutes a spherical shell, the induced magnetic dipole moment only depend on its outer radius. Then the minimal possible dipole moment will be held if all permeable material is found in a sphere with volume V_{fer} since that produces a spherical shell with minimal radius (see Figure 3.4a)

$$\mathbf{m}_{min} = \int_V \mathbf{M} dv = \int_{V_{fer}} \mathbf{M} dv \approx \frac{3V_{fer}}{\mu_0} \mathbf{B}_0. \tag{3.35}$$

The maximal dipole moment will be held if the permeable material constitutes a shield of the object since that produces a spherical shell with maximal radius (see Figure 3.4b)

$$\mathbf{m}_{max} = \int_V \mathbf{M} dv \approx \frac{3V}{\mu_0} \mathbf{B}_0. \tag{3.36}$$

With these two extremities, we can conclude that the induced magnetic dipole

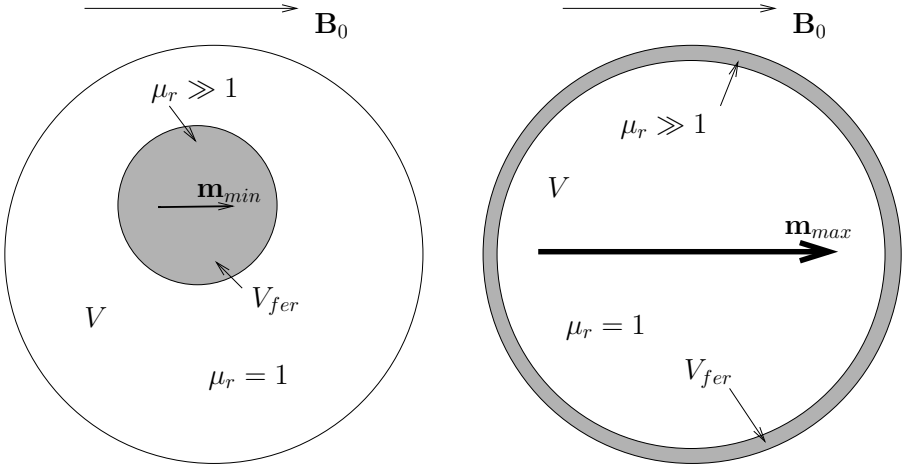

(a) Minimal magnetic dipole moment $\mathbf{m}_{min} = 3V_{fer}/\mu_0$

(b) Maximal magnetic dipole moment $\mathbf{m}_{max} = 3V/\mu_0$

Figure 3.4. An object with volume V contains ferromagnetic material with volume V_{fer} (gray region). The object is applied to a homogeneous magnetic field $\mathbf{B}_0$ and the induced magnetic dipole moment is minimal in Figure 3.4a and maximal in Figure 3.4b since only the outer radius of V_{fer} matter.

moment generally is given by

$$\mathbf{m} \approx \frac{3D}{\mu_0}\mathbf{B}_0 \quad \text{where} \quad V_{fer} \leq D \leq V. \tag{3.37}$$

From this intellectual experiment we have learned that the induced magnetic dipole moment of an object neither reveals its volume V nor the volume of the contained ferromagnetic material, only an lower and a upper limit of these quantities respectively.

A fairly rough but workable approximation is to assume that the relation (3.37) will hold also for other geometrical objects.

For weak applied magnetic fields, the **H**- and **M**-field will reduce to zero when the applied field is removed. However, for strong applied magnetic field the process will not be reversible, which makes permanent magnets possible. Permanently magnetized ferromagnetic substance will therefore also contribute to the total magnetic dipole moment. Unlike the induced magnetic dipole moment presented in (3.34), this dipole moment will have a characteristic orientation in the reference frame of the object and not be oriented in the external applied field.

In order to summarize this section, the magnetic dipole moment $\mathbf{m}$ of a ferromagnetic object in a weak applied homogeneous magnetic field $\mathbf{B}_0$ can be assumed

to be

$$\mathbf{m} = \mathbf{m}_0 + \frac{3D}{\mu_0}\mathbf{B}_0, \tag{3.38}$$

where $\mathbf{m}_0$ is a permanently magnetized dipole vector with a characteristic orientation related to the reference frame of the object and D obeys the relation $V_{fer} \leq D \leq V$, where V_{fer} is the volume of the ferromagnetic substance in the object and V is the volume of the object itself.

3.5 Multipole Expansion

In Section 3.3, the induced magnetic field due to a region of localized current density has been derived resulting in the magnetic dipole. In the derivation of this term, the Taylor expansion of the potential $1/r$ has been truncated (see (3.11)). By going further with this expansion, higher moments of the magnetic vector potential are found. This expansion is known as the multipole expansion. The lth magnetic moment $m_{i_1 \ldots i_l}$ is a symmetric traceless tensor of lth order having $2l+1$ independent components. The magnetic field of the lth multipole may be expressed as (for a derivation, see [9])

$$\mathbf{B}^{(l)}(\mathbf{r}) = \frac{\mu_0}{4\pi}\frac{(2l+1)(\mathbf{r}\cdot\mathbf{M}^{(l)})\mathbf{r} - lr^2\mathbf{M}^{(l)}}{r^{l+4}}, \tag{3.39}$$

where the following vector has been introduced

$$M_i^{(l)} = \sum_{i_1=1}^{3} \cdots \sum_{i_{l-1}=1}^{3} \frac{x_{i_1}\cdots x_{i_{l-1}}}{r^{l-1}}\frac{1}{l!} m_{i i_1 \ldots i_{l-l}}. \tag{3.40}$$

The total magnetic field is then given by

$$\mathbf{B}(\mathbf{r}) = \sum_{l=1}^{\infty} \mathbf{B}^{(l)}(\mathbf{r}). \tag{3.41}$$

The r-dependences of the field for the different multipoles are r^{-3}, r^{-4}, r^{-5} etc. At sufficiently large distances the field is dominated by the dipole term, at shorter distances higher moments will be more important. Generally the series (3.41) can be truncated to arbitrary many multipoles. With a truncation of the pth first multipoles, one gets

$$\mathbf{B}(\mathbf{r}) = \sum_{l=1}^{p} \mathbf{B}^{(l)}(\mathbf{r}) + \mathcal{O}\left(\frac{1}{r^{p+3}}\right), \tag{3.42}$$

since the lowest term not included in the expansion will dominate the truncation error at large distances. Thus, the multipole expansion also gives a hint of how good this truncation is. Furthermore, by setting $p = 1$ one can easily compute the magnetic dipole in (3.16).

3.6 Summary

In order to summarize this chapter, the following statements will be used in the coming modeling work:

- A ferromagnetic object can be modeled as a magnetic dipole if the distance between the object and the observer is large in comparison to the characteristic length of the object (results in (4.4)). In addition, the magnetic dipole moment consists of two differently oriented components (results in (4.7)).
- Two expansions of this model can be considered:
    1. Inspired by the division of ferromagnetic objects into subregions in Figure 3.2a, a grid (or for more oblong objects a row) of dipoles can be considered (results in (4.15)).
    2. The multipole expansion can be used to extend the dipole model (results in (4.17)).

Chapter 4

Modeling

In Chapter 2 and 3 the relevant theory of this thesis has been introduced. Chapter 2 and especially (2.3) gave us the standard form of a time-discrete and time-invariant dynamic system to be used in model based signal processing. Chapter 3 presented the relevant electromagnetic theory, which will be used to derive an explicit expression of (2.3).

In this chapter we will derive an expression how the magnetic field $\mathbf{B}$ varies due to the presence of a moving metallic vehicle. In Section 4.1 the modeling of the motion model (2.3a) will be described, and in Section 4.2 the modeling of the sensor model (2.3b) for point targets is introduced. In Section 2.2 an explicit expression of the batch version of the model is given and in Section 4.4 two different extended target models in batch formulation is presented. The chapter is concluded with a discussion.

4.1 Motion Model

For target tracking a good model describing the motion is necessary. According to Section 2.1, the object is to describe the target dynamics with a model of the form

$$\mathbf{x}_{k+1} = \mathbf{f}(\mathbf{x}_k) + \mathbf{w}_k, \tag{4.1}$$

where $\mathbf{x}_k$ is the state of the system.

In this thesis the objects are vehicle and we will assume a fairly simple motion model. The position $\mathbf{r}_k$ is parameterized by its three Cartesian components $\mathbf{r}_k = [r_k^{(x)}, r_k^{(y)}, r_k^{(z)}]$ and so also the velocity $\mathbf{v}_k = [v_k^{(x)}, v_k^{(y)}, v_k^{(z)}]$. Now, the following *constant velocity model* can be defined

$$\mathbf{r}_{k+1} = \mathbf{r}_k + T_s\mathbf{v}_k + \frac{T_s^2}{2}\mathbf{w}_k \tag{4.2a}$$

$$\mathbf{v}_{k+1} = \mathbf{v}_k + T_s\mathbf{w}_k \tag{4.2b}$$

where $\mathbf{w}_k \sim \mathcal{N}(\mathbf{0}, \mathbf{Q})$ is white Gaussian process noise and T_s is the sample time.

4.2 Sensor Model

The main contribution of this thesis is not the motion model, but the sensor model. In accordance with Section 2.1, it should be on the form

$$\mathbf{y}_k = \mathbf{h}(\mathbf{x}_k) + \mathbf{e}_k \tag{4.3}$$

The sensors to be used are magnetometers, which measures all three Cartesian components of the magnetic field $\mathbf{B}$. The most common application of magnetometers is as a compass. They are a good complement in navigation since they partly reveal their orientation.

However, in this thesis stationary magnetometers will be used. Stationary magnetometers will also mainly measure the magnetic field of the earth. However, as we have seen in Section 3.4, presence of ferromagnetic material near to the sensor adds an induced magnetic field to the measurement. Since a vehicle normally contains a large amount of steel, which is a ferromagnetic material with a relative permeability of $\mu_r \approx 50$ [11], it gives rise to an induced magnetic field. In Section 3.4, we have also learned that this magnetization and its magnetization currents depend on the vehicle orientation in the magnetic field of the earth. In accordance with Section 3.2 we can now verify that the quasi-static approximation holds by considering the following extreme example.

Example 4.1

A large (size $\simeq$ 20 [m]) slalom driving vehicle (frequency $\simeq$ 1 s^{-1}) is traveling through the magnetic field of the earth. Then we have

$$\text{size} \times \text{frequency} = 20 \text{ m} \times 1\text{s}^{-1} = 20 \text{ m/s} \ll c_0$$

Thus, the quasi-static approximation is valid.

Hence, the magnetic field dependency can be found by solving the magnetostatic equations (3.4).

The easiest way to relate the induced magnetic field with the magnetic properties of the vehicle is through its magnetic dipole moment. This relation is given in (3.16). That will give the sensor model

$$\begin{aligned}\mathbf{y}_k &= \mathbf{h}(\mathbf{r}_k, \mathbf{m}_k, \mathbf{B}_0) + \mathbf{e}_k \\ &= \mathbf{B}_0 + \frac{\mu_0}{4\pi}\frac{3(\mathbf{r}_k \cdot \mathbf{m}_k)\mathbf{r}_k - |\mathbf{r}_k|^2\mathbf{m}_k}{|\mathbf{r}_k|^5} + \mathbf{e}_k,\end{aligned} \tag{4.4}$$

where $\mathbf{B}_0$ is the stationary earth magnetic field. In Figure 4.1 the setup is presented. Note that $\mathbf{r}$ in Equation (3.16) has to be replaced with $-\mathbf{r}_k$ (compare Figure 3.1 and Figure 4.1).

According to Equation (3.38), the magnetic dipole moment $\mathbf{m}_k$ consists of two components, one magnetic dipole moment related to the reference frame of the vehicle representing the permanent magnetization $\mathbf{m}_0$, and one oriented in direction of the magnetic field of the earth being the induced magnetic dipole moment. Since the reference frame of the magnetometer is not the same as the

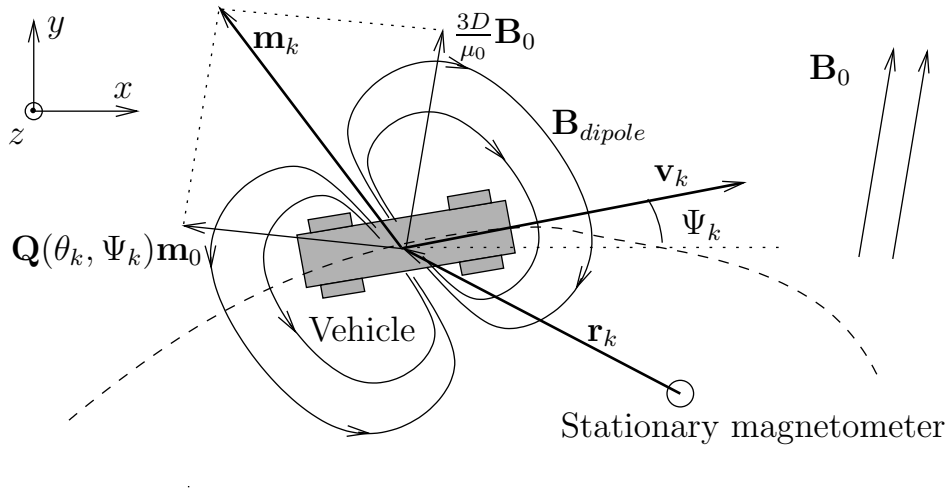

Figure 4.1. A stationary magnetometer measures the magnetic field of the earth $\mathbf{B}_0$ together with an magnetic dipole field $\mathbf{B}_{dipole}$ due to a moving vehicle at position $\mathbf{r}_k$ with velocity $\mathbf{v}_k$ and magnetic dipole moment $\mathbf{m}_k = \mathbf{Q}(\Psi_k, \theta_k)\mathbf{m}_0 + \frac{3D}{\mu_0}\mathbf{B}_0$. The yaw angle Ψ_k is defined by the velocity direction. The pitch angle θ_k is zero if the road is horizontal.

one of the vehicle, a transformation between these two reference frames has to be found. Generally the roll ϕ_k, pitch θ_k and yaw Ψ_k angles are used to define the relative orientation of a vehicle with respect to a reference frame. Here, no roll is assumed and any slip is neglected, i.e. the direction of the velocity vector $\mathbf{v}_k$ uniquely defines the orientation of the vehicle in that

$$\Psi_k = \arctan\left(\frac{v_k^{(y)}}{v_k^{(x)}}\right) \qquad \theta_k = \arctan\left(\frac{v_k^{(z)}}{\sqrt{(v_k^{(x)})^2 + (v_k^{(y)})^2}}\right) \tag{4.5}$$

Now, a vector in the reference of the vehicle can be converted in the reference frame of the magnetometer by the following rotation matrix

$$\mathbf{Q}(\theta_k, \Psi_k) = \mathbf{R}_y(\theta_k)\mathbf{R}_z(\Psi_k) = \begin{pmatrix} \cos\theta_k & 0 & \sin\theta_k \\ 0 & 1 & 0 \\ -\sin\theta_k & 0 & \cos\theta_k \end{pmatrix} \begin{pmatrix} \cos\Psi_k & -\sin\Psi_k & 0 \\ \sin\Psi_k & \cos\Psi_k & 0 \\ 0 & 0 & 1 \end{pmatrix}, \tag{4.6}$$

and we get

$$\mathbf{m}_k = \mathbf{Q}(\theta_k, \Psi_k)\mathbf{m}_0 + \frac{3D}{\mu_0}\mathbf{B}_0, \tag{4.7}$$

where D is a volume characteristic parameter obeying the inequality in (3.37). Note that the approximation in (3.34) will hold since $\mu_r = 50 \gg 1$ for steel.

This sensor model (4.4) can also be seen as a truncation of the series (3.41). Since the signal energy of the signal $\sum \mathbf{y}_k^T \mathbf{y}_k$ is dominated by the dipole term it decays as $\mathcal{O}(\|\mathbf{r}_k\|^{-3})^2$ and the energy of the first neglected term in the series (3.41) decays as $\mathcal{O}(\|\mathbf{r}_k\|^{-4})^2$, the model error to signal ratio decays as

$$\mathcal{O}(\|\mathbf{r}_k\|^{-4})^2 / \mathcal{O}(\|\mathbf{r}_k\|^{-3})^2 = \mathcal{O}(\|\mathbf{r}_k\|^{-2}).$$

Thus, it will be a good far field model. However, it does not take the geometrical extension of the target into account. Therefore, it can be regarded as a point target model.

Furthermore, it is instructive to express (4.4) in spherical coordinates with $\mathbf{m}_k$ being the zenith direction by choosing the following orthonormal basis (see also Figure 4.2)

$$\hat{\boldsymbol{r}}_k = \frac{\mathbf{r}_k}{|\mathbf{r}_k|}, \qquad \hat{\boldsymbol{\alpha}}_k = \frac{\mathbf{r}_k \times \mathbf{m}_k}{|\mathbf{r}_k \times \mathbf{m}_k|}, \qquad \hat{\boldsymbol{\beta}}_k = \hat{\mathbf{r}}_k \times \hat{\boldsymbol{\alpha}}_k \tag{4.8}$$

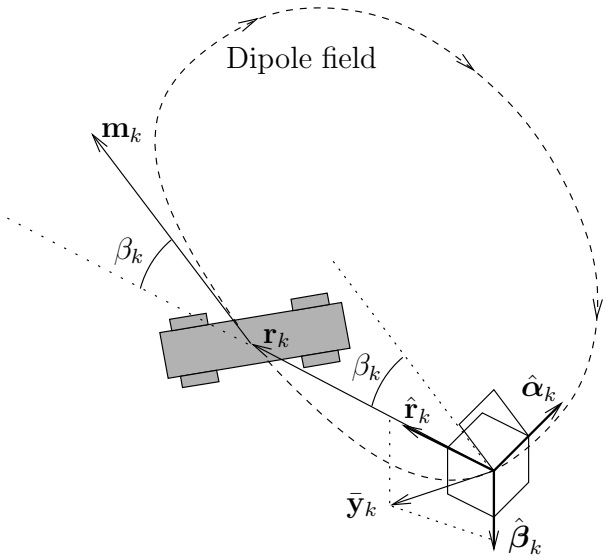

Figure 4.2. The unbiased measurement $\bar{\mathbf{y}}_k$ can be expressed in the orthonormal basis $\hat{\boldsymbol{r}}_k$, $\hat{\boldsymbol{\alpha}}_k$, $\hat{\boldsymbol{\beta}}_k$. The $\hat{\boldsymbol{\alpha}}_k$-coordinate is then zero and the $\hat{\mathbf{r}}_k$- and $\hat{\boldsymbol{\beta}}_k$-coordinates are parameterized with the range $|\mathbf{r}_k|$ and bearing $|\beta_k|$ to the target (see (4.9)).

In this basis, the unbiased measurement $\bar{\mathbf{y}}_k = \mathbf{y}_k - \mathbf{B}_0$ is

$$\tilde{\mathbf{y}}_k = \begin{pmatrix} \tilde{y}_k^{(\hat{\mathbf{r}}_k)} \\ \tilde{y}_k^{(\hat{\boldsymbol{\alpha}}_k)} \\ \tilde{y}_k^{(\hat{\boldsymbol{\beta}}_k)} \end{pmatrix} = \mathbf{A}\bar{\mathbf{y}}_k = \frac{\mu_0}{4\pi} \begin{pmatrix} \frac{2|\mathbf{m}_k|\cos(\beta_k)}{|\mathbf{r}_k|^3} \\ 0 \\ \frac{|\mathbf{m}_k|\sin(\beta_k)}{|\mathbf{r}_k|^3} \end{pmatrix} + \tilde{\mathbf{e}}_k \tag{4.9}$$

$$\text{with} \quad \tilde{\mathbf{e}}_k \sim \mathcal{N}(\mathbf{0}, \mathbf{A}\mathbf{R}\mathbf{A}^T) \quad \text{and} \quad \mathbf{A} = (\hat{\mathbf{r}}_k \ \hat{\boldsymbol{\alpha}}_k \ \hat{\boldsymbol{\beta}}_k)^T, \tag{4.10}$$

where β_k is the angle between $\mathbf{m}_k$ and $\mathbf{r}_k$.

Note that these equations reveal the real information in the three-axis magnetometer. Only a two-dimensional subspace affects the sensor, which is parametrized by the range $|\mathbf{r}_k|$ and the bearing β_k to the target (relative its own magnetic dipole moment). By using (4.9) this range- and bearing-measurement can be found explicitly.

$$|\mathbf{r}_k| = \left(\frac{\mu_0 |\mathbf{m}_k|}{4\pi \sqrt{\left(\frac{1}{2}\tilde{y}_k^{(\hat{\mathbf{r}}_k)}\right)^2 + \left(\tilde{y}_k^{(\hat{\boldsymbol{\beta}}_k)}\right)^2}} \right)^{1/3} \tag{4.11a}$$

$$\beta_k = \arctan\left(\frac{2\tilde{y}_k^{(\hat{\boldsymbol{\beta}}_k)}}{\tilde{y}_k^{(\hat{\mathbf{r}}_k)}} \right) \tag{4.11b}$$

One can compare this sensor model with common sensors in tracking and localization applications that also provide range and bearing information in the context of *signal to noise ratio* (SNR) which is explained in Section 5.4.

- A radar measures range and bearing explicitly, while the magnetometer model provides this information implicitly. It should therefore contain similar information. The radar signal decays as $\mathcal{O}(\|\mathbf{r}_k\|^{-4})$, and the usual thresholding gives a binary SNR (either the target is detected or it is not) which depends on range. The SNR for the magnetometer decays continuously as $\mathcal{O}(\|\mathbf{r}_k\|^{-6})$ and in contrast to a radar, the emitted power of the earth magnetic field cannot be increased to improve SNR.

- Time of arrival (TOA) measures the time of flight between two points, which is linear in range. The signal decays approximately as $\mathcal{O}(\|\mathbf{r}_k\|^{-2})$, and similar to the radar the SNR is quantized in the signal strength.

- Received Signal Strength (RSS) measures the signal level (in dB usually), and this level decays logarithmically in range, so SNR is approximately $\mathcal{O}(-\log(\|\mathbf{r}_k\|))$. The range-measurement (4.11a) resembles RSS in the sense that it does not give a absolute range measure, only a measure which is amplified with the signal strength $|\mathbf{m}_k|$.

4.3 Batched Model

The process noise in the motion model (4.2) allows the vehicle to move and turn in any direction. However, in this thesis special interest will be given to the scenario when vehicles pass the sensor with constant velocities. This prior knowledge enables us to formulate a batch model in accordance with Section 4.3. That is, assume $\mathbf{w}_k = 0$ in (4.2). With this assumption the orientation of the vehicle will be constant and the magnetic dipole moment $\mathbf{m}_k$ will therefore also be constant.

As a consequence, the vehicle specific parameter $\mathbf{m}_0$ and D cannot be revealed, only a linear combination of them given by (4.7). This gives

$$\mathbf{v}_k = \mathbf{v}_0 \tag{4.12a}$$
$$\mathbf{r}_k = \mathbf{r}_0 + kT_s\mathbf{v}_0 \tag{4.12b}$$
$$\mathbf{m}_k = \mathbf{m} \tag{4.12c}$$

By defining

$$\mathbf{h}_k(\mathbf{r}_0, \mathbf{v}_0, \mathbf{m}, \mathbf{B}_0) = \mathbf{h}(\mathbf{r}_0 + kT_s\mathbf{v}_0, \mathbf{m}, \mathbf{B}_0) \tag{4.13}$$

we get the following batched model

$$\begin{aligned}\mathbf{y}_k &= \mathbf{h}_k(\mathbf{r}_0, \mathbf{v}_0, \mathbf{m}, \mathbf{B}_0) + \mathbf{e}_k \\ &= \mathbf{B}_0 + \frac{\mu_0}{4\pi}\frac{3(\mathbf{r}_k \cdot \mathbf{m})\mathbf{r}_k - |\mathbf{r}_k|^2\mathbf{m}}{|\mathbf{r}_k|^5} + \mathbf{e}_k, \quad \text{where} \qquad (4.14a)\\ \mathbf{r}_k &= \mathbf{r}_0 + kT_s\mathbf{v}_0 \qquad (4.14b)\end{aligned}$$

This model is of the form (2.7) and thus a nonlinear weighted least squares estimation can be performed to estimate the parameters $\mathbf{r}_0$, $\mathbf{v}_0$ and $\mathbf{m}$. (See Section 2.3).

4.4 Extended Target Model

In Section 4.2 the point target model of a ferromagnetic vehicle (4.4) has been presented. This sensor model (4.4) is based on the derivation of the magnetic dipole in Section 3.3 where Taylor series in (3.11) has been truncated. This truncation is a good approximation if $r \gg r'$, i.e. if distance to the target is much larger than its geometrical extension. However, if this assumption does not hold, extended target models have to be analyzed. In this section we will present two alternative formulations of such extended target models. One is based on the parameterizing of the target with a row of dipoles and one includes higher order terms of the multipole expansion. As in Section 2.2 only the case with constant velocity will be considered. Thus, only extended target models in batch formulation will be available.

4.4.1 Row of Dipoles

In Section 3.4 we have seen that a magnetized object can be divided into magnetized subregions which has its own characteristic magnetic dipole moments. This idea can also be used to design an extended target sensor model. By dividing the vehicle into smaller subregions, the characteristic length of each subregion will be smaller than the characteristic length of the vehicle and the truncation of (3.11) will be a better approximation. Since a vehicle normally has its largest geometrical extension in the same direction as its course (i.e. its velocity vector $\mathbf{v}_k$), a row of equally distributed dipoles along this direction has been considered (see Figure 4.3). Furthermore, the size of the object is unknown, thus the distance

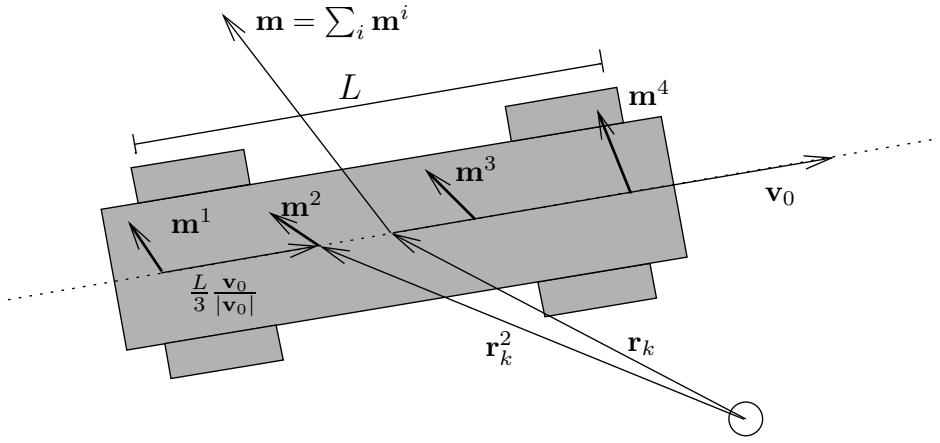

Figure 4.3. The vehicle parametrized with $d = 4$ dipoles aligned in a row in the direction of the vehicle course $\mathbf{v}_0$. All dipoles are equally distanced with the interval $L/(d-1)$, i.e. a total length of L.

between the first and the last dipole L has to be regarded as a state. This results in the following sensor model.

$$\mathbf{y}_k = \mathbf{h}_k(\mathbf{r}_0, \mathbf{v}_0, \mathbf{m}^i, \mathbf{B}_0) + \mathbf{e}_k = \tag{4.15a}$$

$$\mathbf{B}_0 + \sum_{i=1}^{d} \frac{\mu_0}{4\pi} \frac{3(\mathbf{r}_k^i \cdot \mathbf{m}^i)\mathbf{r}_k^i - |\mathbf{r}_k^i|^2 \mathbf{m}^i}{|\mathbf{r}_k^i|^5} + \mathbf{e}_k \quad \text{where} \tag{4.15b}$$

$$\mathbf{r}_k^i = \mathbf{r}_k + (i - \frac{d+1}{2}) \frac{L}{d-1} \frac{\mathbf{v}_0}{|\mathbf{v}_0|} \quad \text{and} \quad \mathbf{r}_k = \mathbf{r}_0 + kT_s\mathbf{v}_0 \tag{4.15c}$$

where $\mathbf{r}_0$, $\mathbf{v}_0$, $\mathbf{m}^i$ and $\mathbf{B}_0$ are regarded as states of the system.

From (3.18) we have learned that the superposition principle for magnetic dipoles is valid. Thus, the relation

$$\mathbf{m} = \sum_{i=1}^{d} \mathbf{m}^i \tag{4.16}$$

couples the states of the extended target model with the states of the point target model. By using this relation the performance of different model orders can be compared.

By setting $d = 1$ this model will coincide with the batch formulation of the point target sensor model (4.14).

4.4.2 Multipoles

Instead of dividing the vehicle into subregions in order to make the truncation of (3.11) for each more valid, higher order terms of (3.11) can be analyzed. This is known as the multipole expansion and is presented in Section 3.5.

$$\mathbf{y}_k = \mathbf{h}_k(\mathbf{r}_0, \mathbf{v}_0, \mathbf{m}^l, \mathbf{B}_0) + \mathbf{e}_k \tag{4.17a}$$

$$\mathbf{B}_0 + \sum_{l=1}^{p} \frac{\mu_0}{4\pi} \frac{(2l+1)(\mathbf{r}_k \cdot \mathbf{M}^l)\mathbf{r}_k - l|\mathbf{r}_k|^2 \mathbf{M}^l}{|\mathbf{r}_k|^{(l+4)}} + \mathbf{e}_k \quad \text{where} \tag{4.17b}$$

$$M_i^l = \sum_{i_1=1}^{3} \cdots \sum_{i_{l-1}=1}^{3} \frac{(x_{i_1})_k \cdots (x_{i_{l-1}})_k}{|\mathbf{r}_k|^{l-1}} \frac{1}{l!} m^l_{i i_1 \ldots i_{l-l}} \quad \text{and} \tag{4.17c}$$

$$\mathbf{r}_k = \mathbf{r}_0 + kT_s \mathbf{v}_0 \tag{4.17d}$$

Here, the following notation has been used

$$\mathbf{M}^l = [M_1^l, M_2^l, M_3^l] \tag{4.18a}$$

$$\mathbf{r}_k = [(x_1)_k, (x_2)_k, (x_3)_k] \tag{4.18b}$$

In this model the state parameter will be $\mathbf{r}_0$, $\mathbf{v}_0$, $\mathbf{m}^l$ and $\mathbf{B}_0$. The lth magnetic moment $\mathbf{m}^l = m^l_{i_1 \ldots i_l}$ is a symmetric traceless tensor of lth order having $2l+1$ independent components.

By setting $p = 1$ this model will coincide with the batch formulation of the point target sensor model (4.14).

4.5 Discussion

In this chapter a point target model as well as extended target models have been provided. Common for all extended target models is the enlargement of the state space. New parameters (degrees of freedom) are added in order to describe the spatial geometry of the target more accurately. However, a large state space dimension will lead to computational difficulties, which complicates a cost efficient real time implementation of the parameter estimation algorithms.

Furthermore, by adding more degrees of freedom to the model the problem with *over modeling* occurs. In the ambition to minimize the residual $\|\hat{\mathbf{y}}_k - \mathbf{y}_k\|$, small deviations of $\mathbf{y}_k$ due to the measurement noise will have an impact of the estimated parameters. Thus, the realization of the measurement noise has been modeled.

Finally, applying a too extended target model does not make any contribution if there are other model uncertainties/errors having a larger impact on the measurement. The following sources of such errors can be considered

- The models introduced in this chapter are all based on an approximative solution of the magnetostatic equations (3.4) for a region of localized current (see Figure 3.1). This means that the vehicle used in this section is assumed to be surrounded with vacuum, and therefore we neglect any presence of other ferromagnetic material near the sensor. For example, the whole ground is assumed to be non-ferromagnetic, which might be a rough approximation.

If all ferromagnetic objects are assumed to be stationary, this would only add a stationary bias to target free data measurements. However, for target data the electromagnetic interaction between the moving ferromagnetic target and other stationary ferromagnetic objects could slightly change the induced magnetic field. The full description can only be found by knowing the ferromagnetic content (i.e. the relative permeability μ_r) at each point in space and solve (3.4) for this more general setup. The problem can be solved by making use of a attenuation map which partly has been done in [3].

- In a multi sensor scenario the relative position and orientation of the sensors are of importance. Any uncertainties of these parameters will have an impact on the estimate.
- In the batch formulation of the point target model as well as in the extended target models the velocity is assumed to be constant. Any deviation from this assumption can be regarded as a model error.

Chapter 5

Magnetometer Potential for Localization and Tracking

In this chapter limitations and possibilities of magnetometer will be discussed in terms of observability and Cramér Rao lower bound as a function of the placement of a second sensor. Also the signal to noise ratio will be computed and analyzed. The discussion will be based on the unbiased batch formulation of the point target sensor model in (4.14) which is

$$\begin{aligned}\bar{\mathbf{y}}_k &= \mathbf{h}_k(\mathbf{r}_0, \mathbf{v}_0, \mathbf{m}) + \mathbf{e}_k \\ &= \frac{\mu_0}{4\pi}\frac{3(\mathbf{r}_k \cdot \mathbf{m})\mathbf{r}_k - |\mathbf{r}_k|^2\mathbf{m}}{|\mathbf{r}_k|^5} + \mathbf{e}_k, \quad \text{where} \qquad (5.1a) \\ \mathbf{r}_k &= \mathbf{r}_0 + kT_s\mathbf{v}_0, \qquad (5.1b)\end{aligned}$$

and $\bar{\mathbf{y}}_k = \mathbf{y}_k - \mathbf{B}_0$. This model is valid for vehicles having constant velocities and where its geometrical extension is small in comparison with the distance between the vehicle and the sensor.

5.1 Single Sensor Observability

To analyze observability, a local analysis can be performed. Consider the covariance of the NLS estimate (2.13c). This is computed by inverting the information matrix

$$\mathcal{I}(\mathbf{x}^0) = \sum_{k=1}^{N} \boldsymbol{\nabla}\mathbf{h}_k^T(\mathbf{x}^0)\mathbf{R}^{-1}\boldsymbol{\nabla}\mathbf{h}_k(\mathbf{x}^0), \qquad (5.2)$$

where $\mathbf{x}^0$ are the true parameters. Any zero eigenvalues of this matrix makes it singular, which indicates a lack of local observability. The unobservable subspace is spanned by the eigenvectors corresponding to the zero eigenvalues, also known as the kernel of the matrix. This kernel can be computed for a specific setup.

Table 5.1. Parameters for a local observability analysis

Parameter		Value		
Initial position	$\mathbf{r}_0[m]$	-3	1	0
Velocity	$\mathbf{v}_0[m/s^2]$	1	0	0
Magn. dipole moment	$\mathbf{m}$	1	1	1
Measurement noise	R	I_3		
Samples	N	60		
Sample time	T_s	0.1		

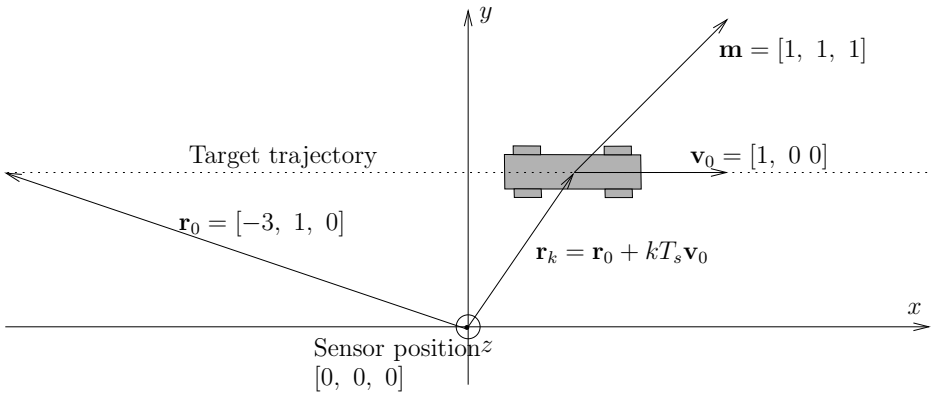

Figure 5.1. Sensor setup for local observability analysis. $\mathbf{r}_0$ is the vector from the sensor to the starting point of the vehicle, $\mathbf{v}_0$ is the velocity of the vehicle and $\mathbf{m}$ is the magnetic dipole moment of the vehicle.

Consider the following parameters in Table 5.1. This will generate a scenario where the target is starting at $[-3,\ 1,\ 0]$, following the x-axis and ending at $[3,\ 1,\ 0]$ (see Figure 5.1).

By parameterization $\mathbf{x}^0 = [\mathbf{r}_0,\ \mathbf{v}_0,\ \mathbf{m}]^T$ and computing the eigenvalues of the information matrix (5.2), this will result in *one* eigenvalue having significantly less magnitude than the other eigenvalues (see Figure 5.2). The corresponding eigenvector is $[-3,\ 1,\ 0,\ 1,\ 0,\ 0,\ 3,\ 3,\ 3]^T$, which equals $[\mathbf{r}_0,\ \mathbf{v}_0,\ 3\mathbf{m}]^T$. This property is not unique for the chosen $\mathbf{x}^0$. In fact, it can be shown that $\mathcal{I}(\mathbf{x}^0) \cdot [\mathbf{r}_0,\ \mathbf{v}_0,\ 3\mathbf{m}]^T = \mathbf{0}$ for all $\mathbf{x}^0 \in \mathbb{R}^9$. Thus, the kernel is generally given by the following one-dimensional subspace:

$$\mathrm{Ker}(\mathcal{I}(\mathbf{x}^0)) = (\lambda[\mathbf{r}_0,\ \ \mathbf{v}_0,\ 3\mathbf{m}]^T \mid \lambda \in \mathbb{R}) \tag{5.3}$$

However, due to the non-linearity, this expression of the unobservable subspace is only valid at the point $\mathbf{x}^0$ and can therefore only be regarded as the tangent of the unobservable one-dimensional manifold at this point. Denote this manifold $\mathbf{X}(u) = [\mathbf{R}_0(u),\ \mathbf{V}_0(u),\ \mathbf{M}(u)]^T$, where u is a scalar parameter. For each u there

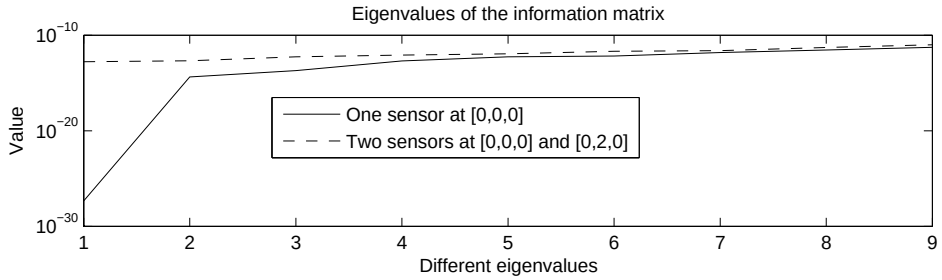

Figure 5.2. The eigenvalues of the information matrix for the setup presented in Table 5.1 being observed with 1) one sensor at $[0,0,0]^T$ and 2) two sensors at $[0,0,0]^T$ and $[0,2,0]^T$

will be a $\lambda(u)$ such that

$$\frac{d}{du}\mathbf{X}(u) = \frac{d}{du}\begin{pmatrix} \mathbf{R}_0(u) \\ \mathbf{V}_0(u) \\ \mathbf{M}(u) \end{pmatrix} = \lambda(u)\begin{pmatrix} \mathbf{R}_0(u) \\ \mathbf{V}_0(u) \\ 3\mathbf{M}(u) \end{pmatrix} \tag{5.4}$$

By choosing the parameterization $u = \lambda(u)^{-1}$, we get the following unobservable manifold

$$\mathbf{X}(u) = \begin{pmatrix} u\mathbf{r}_0 \\ u\mathbf{v}_0 \\ u^3\mathbf{m} \end{pmatrix} \tag{5.5}$$

It is instructive to substitute $\mathbf{X}(u)$ into (5.1) and conclude that each $\mathbf{h}_k(\mathbf{X}(u))$ is independent of the parameter u, which means that all points on this manifold will give the same output $\mathbf{y}_k$. For example, multiplying $\mathbf{r}_0$ and $\mathbf{v}_0$ with 2, and $\mathbf{m}$ with $2^3 = 8$ will result in the same output $\mathbf{y}_k$.

The result is physically quite intuitive since the magnetometer does not measure any absolute distances and the system can be arbitrarily scaled without changing the measured output. Thus, a small vehicle driving slowly close to the sensor will give rise to the same signal as a large vehicle driving fast far from the sensor. Since the magnetic dipole moment $\mathbf{m}$ is related to the volume of the vehicle, the cubic scaling of this parameter in comparison to the distance $\mathbf{r}_0$ and the velocity $\mathbf{v}_0$ is explained.

Furthermore, from the expression (5.5) we can conclude that the magnitudes of the vectors $\mathbf{r}_0$, $\mathbf{v}_0$ and $\mathbf{m}$ cannot be uniquely determined, only a non-linear combination of them. However, their directions are still observable.

5.2 Multi Sensor Observability

The lack of observability can be solved with a second sensor. To handle multiple sensors, the sensor model has to be slightly expanded. Let the jth sensor be

positioned at $\boldsymbol{\theta}_j$. The target parameter relative to the the jth sensor will then be $\mathbf{x}_j = [\mathbf{r}_0 - \boldsymbol{\theta}_j,\ \mathbf{v}_0,\ \mathbf{m}]^T$. The total sensor model is then given by

$$\mathbf{y}_{k,j} = \mathbf{h}_k(\mathbf{x}_j) + \mathbf{e}_{k,j} \quad \text{for all } j \in J \tag{5.6}$$

Furthermore, in a multi-sensor scenario, the information matrices for all sensors are additive, so

$$\mathcal{I}_{tot}(\mathbf{x}^0,\ \boldsymbol{\theta}_{1:J}) = \sum_{j=1}^{J} \mathcal{I}(\mathbf{x}_j^0) \tag{5.7}$$

Now, to the unobservable sensor setup presented in Table 5.1 a second sensor can be added. By computing the total information matrix it can be concluded that its eigenvalues are all non-zero (see Figure 5.2) and with that, the system is observable. The concept of observability can be extended by not only distinguishing between zero and non-zero eigenvalues, but also comparing their magnitudes. The design goal in the sensor deployment is then to get all eigenvalues of the same order of magnitude to get the best possible observability. This property is measured by the condition number of the information matrix $\kappa(\mathcal{I}_{tot}(\mathbf{x}^0,\ \boldsymbol{\theta}_{1:J}))$, which for a positive symmetric matrix can be expressed as

$$\kappa(A) = \frac{\lambda_{max}(A)}{\lambda_{min}(A)}, \tag{5.8}$$

where $\lambda_{max}(A)$ and $\lambda_{min}(A)$ are maximal and minimal eigenvalues of A respectively. A low condition number indicates that the system has good observability properties and its optimal value is 1.

In order to examine where a second magnetometer should be placed to get the most well-conditioned information matrix, the condition number can be computed for different positions $\boldsymbol{\theta}_2$ of the second sensor. A plot illustrating this is presented in Figure 5.3. It can be concluded that the optimal sensor deployment of a two sensor system is to locate them symmetrically at both sides of the target trajectory. If the sensors due to practical reasons must be located at the same side of the trajectory, they should be well separated, which is intuitive (however, presumably not too separeded!).

5.3 Cramér Rao Lower Bound

CRLB (see Section 2.4) is related to observability, in that it applies a local analysis and basically approximates $V(\hat{\mathbf{x}})$ with a quadratic function $V(\hat{\mathbf{x}}) \approx \hat{\mathbf{x}}^T \mathcal{I}(\mathbf{x}^0)\hat{\mathbf{x}}$, where $\mathcal{I}(\mathbf{x}^0)$ is the FIM, which for this problem is given by (5.2). The CRLB states that any unbiased estimate must have a covariance matrix larger than or equal to the inverse of the FIM

$$\mathrm{Cov}(\hat{\mathbf{x}}) \geq \mathcal{I}(\mathbf{x}^0)^{-1} \tag{5.9}$$

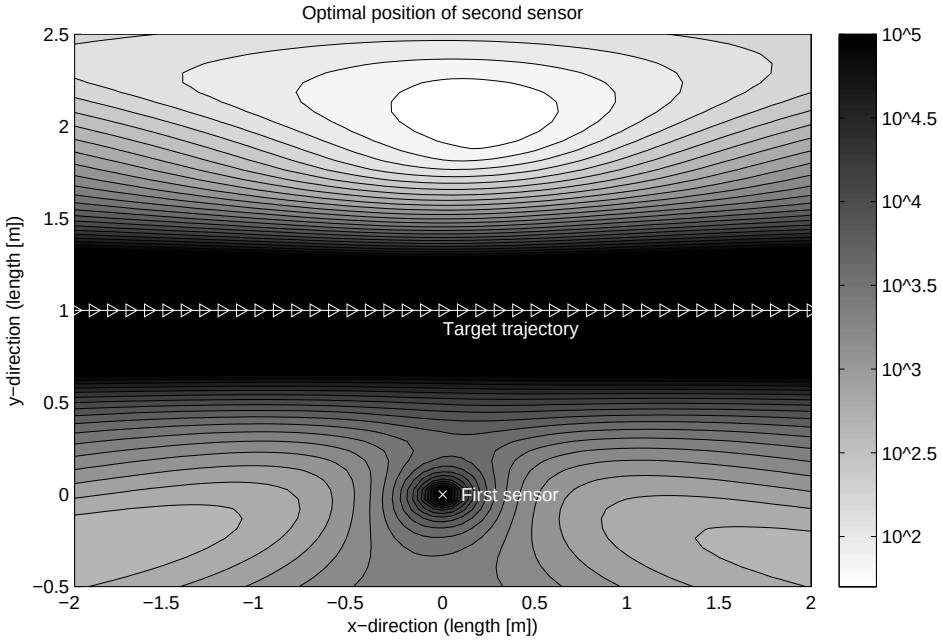

Figure 5.3. The condition number of the information matrix $\kappa(\mathcal{I}_{tot}(\mathbf{x}^0, \boldsymbol{\theta}_{1:2}))$ as a function of the location of the second sensor $\boldsymbol{\theta}_2$ in the x-y-plane where $\mathbf{x}^0$ is given by the setup presented in Table 5.1 and $\boldsymbol{\theta}_1 = [0, 0, 0]^T$.

The design goal of the sensor deployment in the context of CRLB is then to maximize $\mathcal{I}(\mathbf{x}^0)$ since that will minimize the covariance matrix $\mathrm{Cov}(\hat{\mathbf{x}})$. This is achieved by minimizing

$$||\mathrm{Cov}(\hat{\mathbf{x}})||_2 \approx ||\mathcal{I}(\mathbf{x}^0)^{-1}||_2 = \frac{1}{\lambda_{min}(\mathcal{I}(\mathbf{x}^0))}. \tag{5.10}$$

However, since the goal of this sensor deployment analysis is to find the optimal sensor positions relative to each other and the target trajectory, and not to get optimal absolute positions of the sensors (this would be achieved by localizing the sensors as close as possible to the target!), the parameters must be meaningfully normalized. By defining the characteristic length of the problem r as being the shortest euclidean distance from the target trajectory to the nearest sensor, we can introduce the following dimensionless parameters

$$\tilde{\mathbf{r}}_0 = \frac{\mathbf{r}_0}{r} \tag{5.11a}$$

$$\tilde{\mathbf{v}}_0 = \frac{\mathbf{v}_0}{r/T} \tag{5.11b}$$

$$\tilde{\mathbf{m}} = \frac{\mathbf{m}}{1} \tag{5.11c}$$

Consequently the measurements $\mathbf{y}$ and $\mathcal{I}(\mathbf{x}^0)$ will be scaled accordingly

$$\tilde{\mathbf{y}} = r^3\mathbf{y} \tag{5.12a}$$
$$\mathcal{I}(\tilde{\mathbf{x}}^0) = r^6\mathcal{I}(\mathbf{x}^0). \tag{5.12b}$$

From this we get

$$||\mathrm{Cov}(\hat{\tilde{\mathbf{x}}})||_2 \approx \frac{1}{\lambda_{min}(r^6\mathcal{I}(\mathbf{x}^0))} = \frac{r^{-6}}{\lambda_{min}(\mathcal{I}(\mathbf{x}^0))} \tag{5.13a}$$
$$\sim \frac{\lambda_{max}(\mathcal{I}(\mathbf{x}^0))}{\lambda_{min}(\mathcal{I}(\mathbf{x}^0))} = \kappa(\mathcal{I}(\mathbf{x}^0)) \tag{5.13b}$$

since $\mathcal{I}(\mathbf{x}^0)$ decays as the signal to noise ratio, which decays as $\mathcal{O}(r^{-6})$.

Thus, a small condition number of the information matrix will ensure a small covariance (after normalization). Therefore, the assumption in Section 5.2 that the optimal sensor deployment is measured by the condition number of the information matrix is also valid in the context of CRLB.

5.4 Signal to Noise Ratio

One main problem of using magnetometers for tracking is their limited range and in this section we will estimate this range by comparing the signals strength with the measurement noise.

We can define the *Signal to Noise Ratio* (SNR) as

$$\mathrm{SNR} = \mathbf{h}^T(\mathbf{x})\mathbf{R}^{-1}\mathbf{h}(\mathbf{x}). \tag{5.14}$$

SNR can be interpreted as an energy ratio between the signal an the noise. Further, note that

$$\bar{\mathbf{y}}_k^T\mathbf{R}^{-1}\bar{\mathbf{y}}_k \sim \chi_3^2(\mathrm{SNR}), \tag{5.15}$$

where $\chi_3^2(\mathrm{SNR})$ is a non-central chi-square distribution with 3 degrees of freedom and with SNR as the non-centrality parameter.

For targets very far away, the sensor measures only noise, and this quantity becomes a standard χ_3^2 distribution. The larger the SNR, the more information of the target is available.

In order to detect a target from one measurement $\mathbf{y}_k$, the following test quantity can be considered

$$T(\bar{\mathbf{y}}_k) = \bar{\mathbf{y}}_k^T\mathbf{R}^{-1}\bar{\mathbf{y}}_k \sim \begin{cases} \chi_3^2 & \text{under } H_0 \\ \chi_3^2(\mathrm{SNR}) & \text{under } H_1 \end{cases} \tag{5.16}$$

where

$$H_0 \ : \ \bar{\mathbf{y}}_k = \mathbf{e}_k \tag{5.17a}$$
$$H_1 \ : \ \bar{\mathbf{y}}_k = h(\mathbf{x}_k) + \mathbf{e}_k. \tag{5.17b}$$

If a false alarm rate $P_{FA} = P(T(\bar{\mathbf{y}}_k) => h|H_0)$ of 1% can be accepted we get

$$P(\chi_3^2 > h) = 0.01 \quad \Rightarrow \quad h = 11.2 \tag{5.18}$$

In order to detect half of the targets, the detection rate $P_D = P(T(\bar{\mathbf{y}}_k) > h|H_1)$ must be 50% and

$$P(\chi_3^2(\text{SNR}) \geq 11.2) = 0.5 \quad \Rightarrow \text{SNR} > 9.2 \tag{5.19}$$

This means, the signal contains 9.2 times more energy than the noise. The distribution of the test statistic under these assumptions is presented in Figure 5.4.

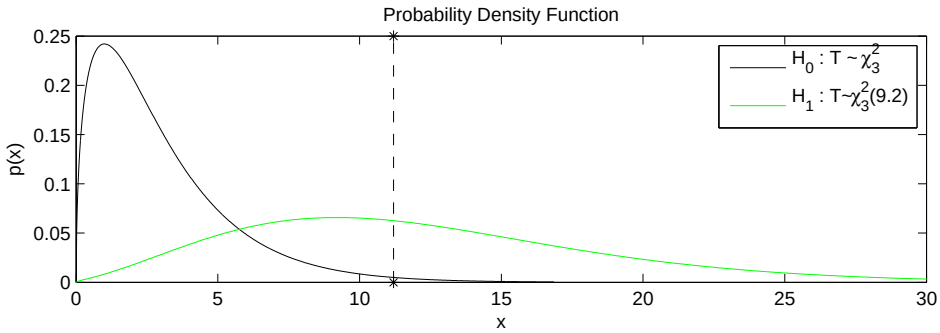

Figure 5.4. The distribution of the test statistic for one measurement $\bar{\mathbf{y}}_k$ and with SNR = 9.2 under H_0 and H_1 respectively. The threshold h for $P_{FA} = 0.01$ and $P_D = 0.5$ is marked with a vertical dashed line.

Furthermore, we know from (4.4) that

$$\|\mathbf{h}(\mathbf{x}_k)\| \approx \frac{\mu_0}{4\pi} \frac{\|\mathbf{m}\|}{\|\mathbf{r}_k\|^3} \tag{5.20}$$

and thus

$$\text{SNR}(\|\mathbf{r}_k\|, \|\mathbf{m}_k\|, \|\mathbf{R}\|) \approx \left(\frac{\mu_0}{4\pi}\right)^2 \frac{\|\mathbf{m}\|^2}{\|\mathbf{R}\| \cdot \|\mathbf{r}_k\|^6} \tag{5.21}$$

For the sensors and targets presented in Section 6, typical values of $\|\mathbf{m}_k\|$ and $\|\mathbf{R}\|$ are

$$\|\mathbf{m}_k\| \approx 1 \qquad \|\mathbf{R}\| \approx 10^{-21} \tag{5.22}$$

which gives

$$\text{SNR}(\|\mathbf{r}_k\|) \approx \left(\frac{\mu_0}{4\pi}\right)^2 \frac{\|\mathbf{m}\|^2}{\|\mathbf{R}\|^2 \|\mathbf{r}_k\|^6} = \frac{10^7}{\|\mathbf{r}_k\|^6} \tag{5.23}$$

With the inequality (5.19) we get

$$\|r_k\| \lesssim 10 \text{ [m]} \tag{5.24}$$

Thus, the usage of magnetometers for detecting and tracking vehicles is limited to a range of approximately 10 meters. However, for an automated traffic surveillance system this is enough for tracking vehicles in a certain intersection. In order to track vehicles in a larger area, a sensor network of spatially distributed magnetometers can be considered.

Chapter 6

Sensor Model Validation

In Chapter 4 a point target sensor model as well as extended target sensor models have been derived. In order to validate these sensor models, real experimental data has been collected with magnetometers. The sensor model validation presented in this chapter will only consider data collected from vehicles having constant velocities. Thus, only the batch formulation in (4.14) and the corresponding extended target models (4.15) and (4.17) will be considered and the initial position $\mathbf{r}_0$, the velocity $\mathbf{v}_0$ and the magnetic dipole moment $\mathbf{m}$ can be estimated with Algorithm 1. Furthermore, the relation between $\mathbf{m}$ and the vehicle orientation in (4.7) will be validated by measuring this quantity for the same car heading in different compass directions. In accordance with the results in Section 5.1 and 5.2 all measurements have been done with two sensors in order to reach observability for the model (4.14).

6.1 The Sensors

For the real experimental data collection two MTi Xsens sensors [16] have been used (see Figure 6.1). Each sensor contains gyroscopes, accelerometers and magnetometers in 3D. The most common user scenario for this combination of sensors is as an IMU for stabilization and control of cameras, robots, vehicles and other (un)manned equipment. However, we are only interested in using it as a stationary sensor where the magnetometer measurements are of main importance. In addition, the accelerometer measurements will be used for calibrating the sensor orientation.

6.2 Experimental Setup

The two magnetometers have been placed close to a straight road (see Figure 6.2) According to Figure 5.3 they should be deployed symmetrically at each side of the road. In the experimental setup a relative distance of 9 meters between the sensors has been used, which results in a minimum length of ~ 4.5 meters to the

Figure 6.1. Xsens MTi contains gyroscopes, accelerometers and magnetometers in 3D.

targets. According to (5.23) this gives a SNR of

$$\mathrm{SNR}(\|\mathbf{r}_k\|) \approx \frac{10^7}{\|4.5|^6} \approx 1200 \tag{6.1}$$

i.e. the signal has 1200 times more energy than the noise when the vehicle is at closest, which is a very good SNR. As reference data a video camera has been

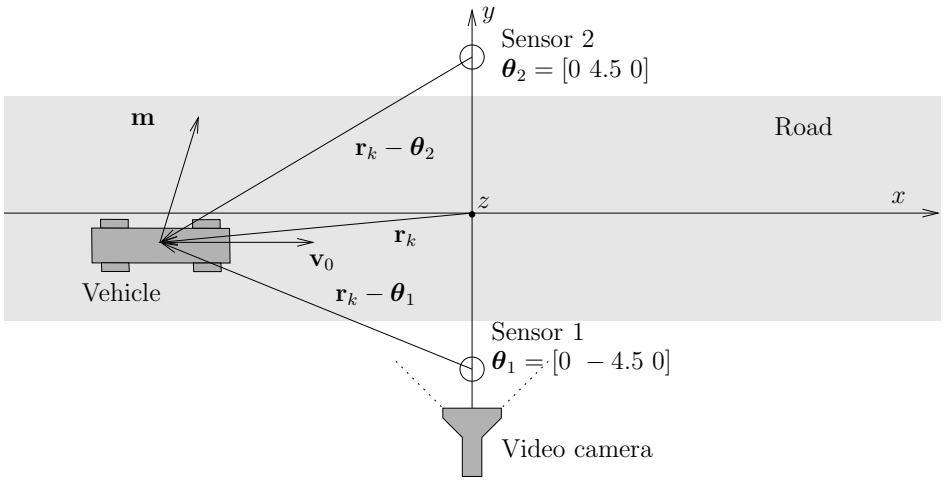

Figure 6.2. Sensor setup for the sensor model validation. $\mathbf{r}_k$ is a vector from the origin to the vehicle, $\mathbf{v}_0$ is the velocity of the vehicle, $\mathbf{m}$ is the magnetic moment of the vehicle and $\boldsymbol{\theta}_1/\boldsymbol{\theta}_2$ are the positions of the two sensors.

used recording all objects within the sensor range area. A north-south reference

road has been chosen for the experimental data collection (see Figure 6.3). The collected raw data after monitoring the traffic in $\sim$ 10 minutes is presented in Figure 6.4.

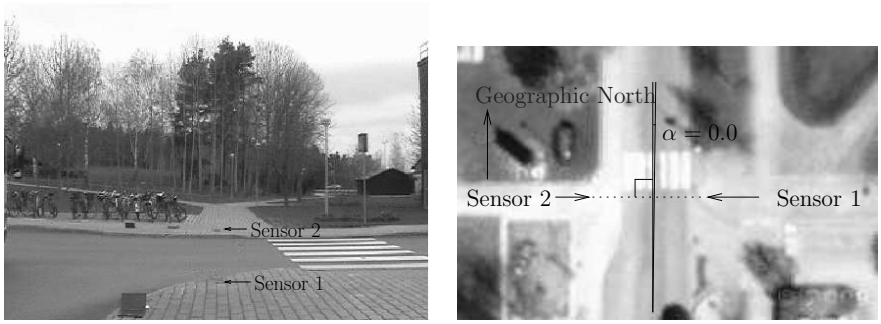

(a) From the side (b) From above

Figure 6.3. The sensor setup seen from the side and above for the chosen north-south reference road. α is the angle between the north-south direction and the road, which is $\alpha = 0.0^\circ$ for this particular road.

6.3 Preprocessing of Sensor Data

Before the raw data presented in Figure 6.4 can be processed in the NLS framework as presented in Algorithm 1, some preprocessing steps have to be performed:

1. *Synchronization* - The data from the two sensors has to be synchronized. Due to technical limitations, two asynchronous data collection equipments for the two sensors have been used. The synchronization has been solved by simultaneously knocking at the two sensors. The time lag could then be found with a correlation analysis of the accelerometer data from the sensors.

2. *Decimation* - The data has been collected at a sample rate of 100 Hz. However, this is more than needed. Thus, the data has been anti-alias filtered and down-sampled to 12.5 Hz.

3. *Sensor orientation calibration* - With two 3D-sensors it is crucial that they have the same reference frame. The calibration of this reference frame can be performed using the accelerometer and making use of the magnetometer as a compass.

4. *Noise distribution* - The noise distribution of the sensors has to determined. This has been done by estimating the covariance of target free data.

5. *Target detection* - The relevant target scenarios in the raw data has to be identified. Due to a fairly good SNR this could be done by thresholding of the signal energy.

Steps 3 and 4 will be described in more detail in the following subsections.

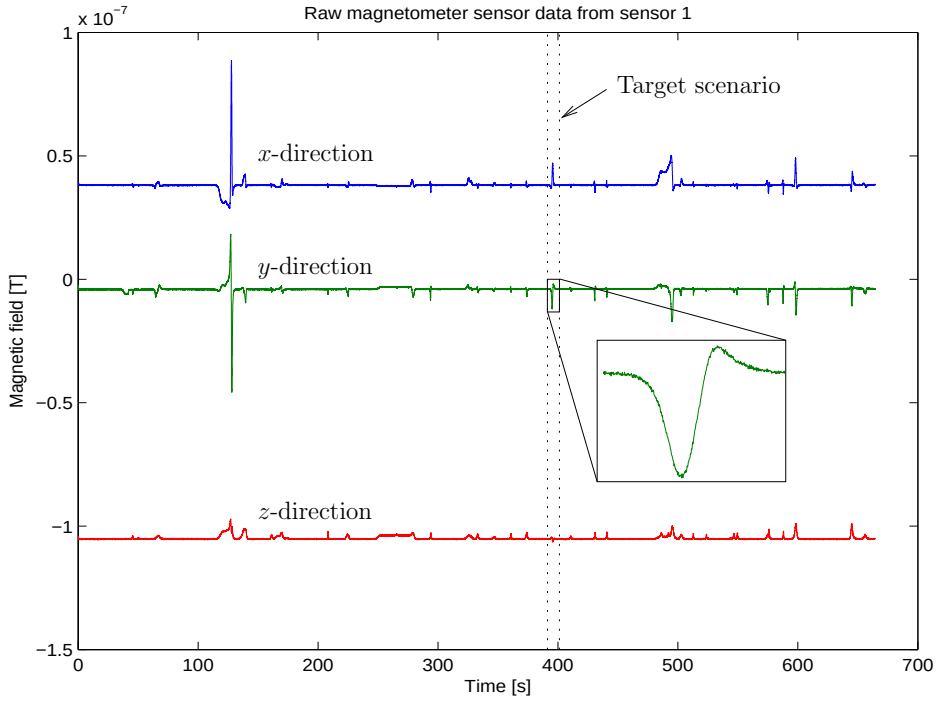

Figure 6.4. Raw sensor data collected with a magnetometer close to the road (see Figure 6.3). Mainly the magnetometer measures the magnetic field of earth. However, small deviations will occur when a vehicle passes by. All deviations in the figure represent a target (the big one to the left is a bicycle passing very close to the sensor). One target scenario is marked with vertical lines and an enlarged copy of the y-component for that scenario is provided (see the small figure).

6.3.1 Sensor Orientation Calibration

Even though the sensor orientation has been adjusted manually in accordance with the reference frame presented in Figure 6.2, a perfect result can not be assumed. However, the accelerometer and the target free magnetometer measurements reveal the true orientation of the sensor.

The accelerometer measures proper acceleration (the acceleration experienced relative to free fall) which always points in zenith direction in the stationary case. In order to get the measured acceleration $\mathbf{a}$ to point in zenith direction, all data has to be rotated (see Figure 6.5a). This can be achieved by rotating with the angle θ

$$\cos\theta = \left(\frac{\mathbf{a}}{||\mathbf{a}||} \cdot \begin{pmatrix} 0 \\ 0 \\ 1 \end{pmatrix} \right) = \frac{a_z}{||\mathbf{a}||} \tag{6.2}$$

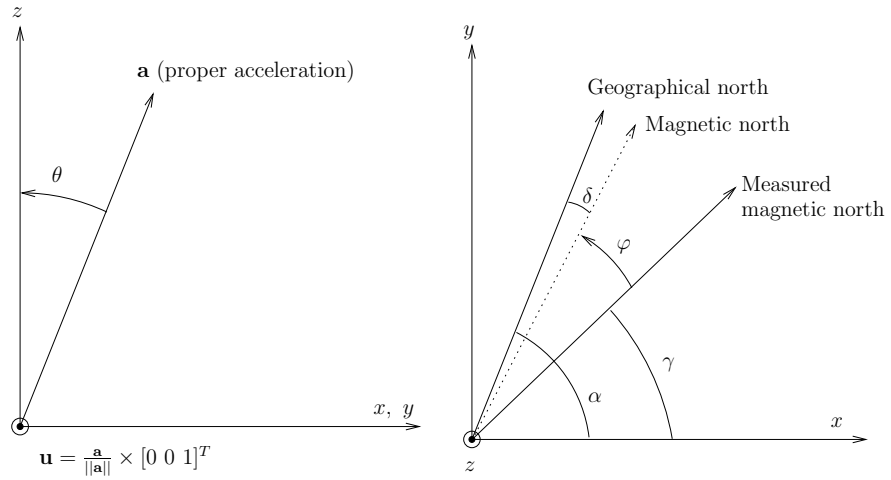

(a) The sensor data is rotated around the axis $\mathbf{u} = \mathbf{a}/||\mathbf{a}|| \times (0\ 0\ 1)^T$ by the angle θ to align the accelerometer measurement in the zenith direction.

(b) The sensor data is rotated around the z-axis by the angle φ to align the measured magnetic north with the true magnetic north.

Figure 6.5. Rotations orthogonal to and parallel with the z-axis to transform the sensor data in the reference frame presented in Figure 6.2.

around the axis

$$\mathbf{u} = \frac{\mathbf{a}}{||\mathbf{a}||} \times \begin{pmatrix} 0 \\ 0 \\ 1 \end{pmatrix} = \frac{1}{||\mathbf{a}||} \begin{pmatrix} a_y \\ -a_x \\ 0 \end{pmatrix} \tag{6.3}$$

Now, Rodrigues' rotation formula can be used to define the desired rotation matrix

$$\mathbf{R}_\mathbf{u}(\theta) = \mathbf{u}\mathbf{u}^T + (I - \mathbf{u}\mathbf{u}^T)\cos\theta + \mathbf{Q}\sin\theta, \tag{6.4}$$

where

$$\mathbf{Q} = \begin{pmatrix} 0 & -u_z & u_y \\ u_z & 0 & -u_z \\ -u_y & u_z & 0 \end{pmatrix}. \tag{6.5}$$

Furthermore, a correct orientation in the x-y-plane is desired. For this purpose the magnetometer can be used as a compass. Without presence of metallic objects, the x and y component of the magnetometer measurement points out the magnetic north. Due to magnetic declination the magnetic north slightly deviates from the geographic north. In Linköping in April 2010 this declination was $\delta = 3°48' = 3.8°$ easterly [5]. Furthermore, according to Figure 6.2 the x-direction of the sensor reference frame should be parallel to the road, of which geographical orientation can be found with a map. In this experiment a north-south reference road has been used, i.e. $\alpha = 0.0$ (see Figure 6.3b). In order to orientate the data in the

global reference frame (see Figure 6.5b), it has to be rotated around the z-axis with the angle

$$\varphi = \alpha - \delta - \gamma \tag{6.6}$$

where γ is the angle to the measured magnetic north found by computing

$$\gamma = \arctan\left(\frac{B_0^{(y)}}{B_0^{(x)}}\right), \tag{6.7}$$

where $\mathbf{B}_0$ is the measured magnetic field without targets after having applied the first rotation $\mathbf{R_u}(\theta)$. The rotation matrix rotating the angle φ around the the z-axis can also be found with the Rodrigues' rotation formula to be

$$\mathbf{R_z}(\varphi) = \begin{pmatrix} \cos\varphi & -\sin\varphi & 0 \\ \sin\varphi & \cos\varphi & 0 \\ 0 & 0 & 1 \end{pmatrix}. \tag{6.8}$$

Thus, sensor orientation can be calibrated by using the transformation

$$\tilde{\mathbf{y}}_k = \mathbf{R_z}(\varphi)\mathbf{R_u}(\theta)\mathbf{y}_k. \tag{6.9}$$

6.3.2 Noise Distribution

Without any targets, the magnetometer measures only the present homogeneous magnetic field (the magnetic field of the earth) together with measurement noise. According to [14], the noise of the magnetometer [16] is white Gaussian, i.e. its samples are i.i.d. and normal distributed with zero mean. Such a stochastic process is uniquely defined by its covariance matrix $\mathbf{R}_j$. These two symmetric 3×3 -matrices R_1 and R_2 for the two sensors in use are estimated to be

$$\mathbf{R}_1 = 10^{-21} \begin{pmatrix} 0.6434 & -0.0360 & -0.0561 \\ -0.0360 & 0.5489 & 0.0578 \\ -0.0561 & 0.0578 & 0.7692 \end{pmatrix}, \tag{6.10a}$$

$$\mathbf{R}_2 = 10^{-21} \begin{pmatrix} 0.7408 & 0.1012 & 0.1064 \\ 0.1012 & 0.9564 & 0.1531 \\ 0.1064 & 0.1531 & 0.7325 \end{pmatrix}, \tag{6.10b}$$

where the unit of the measurement is Tesla.

6.4 Point Target Model Validation

After having preformed the steps presented in Section 6.3, the NWLS methodology in Section 2.3 can be applied to estimate the parameters $\mathbf{r}_0$, $\mathbf{v}_0$, $\mathbf{m}$ and $\mathbf{B}_0$ for the batch model (4.14). To handle multiple sensors, (4.14) has to be slightly redefined by introducing

$$\mathbf{h}_{k,j}(\mathbf{r}_0, \mathbf{v}_0, \mathbf{m}_0) = \mathbf{h}_k(\mathbf{r}_0 - \boldsymbol{\theta}_j, \mathbf{v}_0, \mathbf{m}_0), \tag{6.11}$$

where $\boldsymbol{\theta}_1$ and $\boldsymbol{\theta}_2$ are the positions of the two sensors. An estimate of the parameter $\mathbf{x} = [\mathbf{r}_0,\ \mathbf{v}_0,\ \mathbf{m}]$ can now be solved by considering the system

$$\mathbf{y}_{k,j} = \mathbf{h}_{k,j}(\mathbf{x}) + \mathbf{e}_{k,j}, \tag{6.12}$$

and solving

$$\hat{\mathbf{x}} = \arg\min_{\mathbf{x}} V(\mathbf{x}) \tag{6.13a}$$

$$V(\mathbf{x}) = \sum_{k=1}^{N}\sum_{j=1}^{2}(\mathbf{y}_{k,j} - \mathbf{h}_{k,j}(\mathbf{x}))^T\mathbf{R}_j^{-1}(\mathbf{y}_{k,j} - \mathbf{h}_{k,j}(\mathbf{x})). \tag{6.13b}$$

According to (2.13), we also get a covariance estimate

$$\mathrm{Cov}(\hat{\mathbf{x}}) \approx \left(\sum_{k=1}^{N}\sum_{j=1}^{2}\boldsymbol{\nabla}\mathbf{h}_{k,j}(\hat{\mathbf{x}})^T\mathbf{R}_j^{-1}\boldsymbol{\nabla}\mathbf{h}_{k,j}(\hat{\mathbf{x}})\right)^{-1}. \tag{6.14}$$

(6.13) can now be solved with the Levenberg-Maquardt algorithm (see Algorithm 1) and the result is summarized in Table 6.1, 6.2, 6.3 and 6.4 for each vehicle presented in Figure 6.6.

6.4.1 Model Validation

Note that the cost function $V(\hat{\mathbf{x}})$ is $\chi^2_{Nn_y-n_x}$ distributed given that the sensor model (both $\mathbf{h}_{k,j}(\mathbf{x})$ and $\mathbf{e}_{k,j} \sim \mathcal{N}(\mathbf{0}, \mathbf{R}_j)$) is correct, n_y and n_x being the dimension of each measurement and the state space respectively. Therefore, if the normalized cost function $V(\hat{\mathbf{x}})/(Nn_y - n_x) \approx 1$, then this would indicate a correct model.

Table 6.1. The values of the normalized cost function for the point target model.

Vehicle	$V(\hat{\mathbf{x}})/(Nn_y - n_x)$	N	n_y	n_x
1	360	70	6	15
2	142	54	6	15
3	10	32	6	15
4	14	44	6	15
5	51	27	6	15
6	17	22	6	15

In Table 6.1 the normalized cost function for the vehicles in Figure 6.6 is presented. By this we can conclude that larger vehicles generally produce a worse fit with the measured data than smaller vehicles. This is intuitively clear since the point target model assumes that the target has no geometrical extension, which is a more rough approximation for large vehicles than for small vehicles. However, for all vehicles, the normalized cost function is much larger than 1.

(a) Vehicle 1

(b) Vehicle 2

(c) Vehicle 3

(d) Vehicle 4

(e) Vehicle 5

(f) Vehicle 6

Figure 6.6. The vehicles used in the sensor model validation.

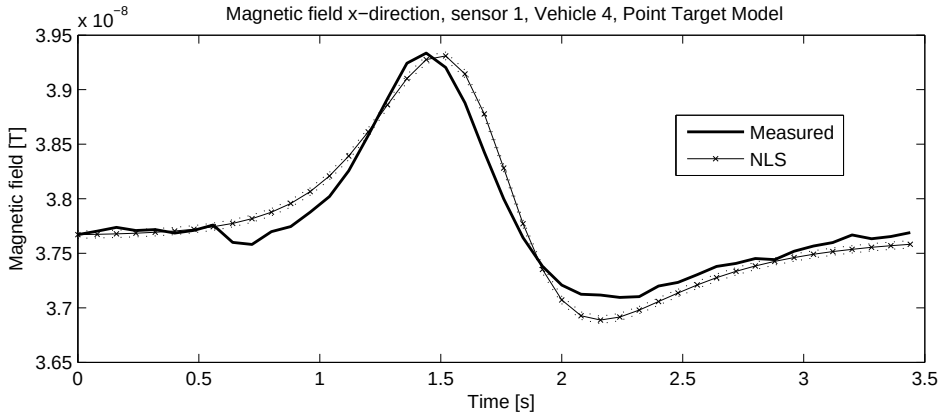

Figure 6.7. The measured magnetic field $y_{k,1}^{(x)}$ in the x-direction together with the NLS-estimated value $h_{k,1}^{(x)}(\hat{\mathbf{x}})$ for vehicle 4 and sensor 1 with a 90 % confidence interval. For the nonlinear transformation $h_{k,1}^{(x)}(\hat{\mathbf{x}})$ a first order Taylor approximation has been used.

6.4.2 Initial Position Estimation

Table 6.2. The estimated initial position $\hat{\mathbf{r}}_0$ in Cartesian coordinates (xyz) for the point target model with standard deviations in parenthesis. Also reference data for the three Cartesian coordinates is given. For example, for Vehicle 1 the x-component of $\hat{\mathbf{r}}_0$ is -12.72 meters with a standard deviation of 0.03 meters and according to the reference data this parameter should be negative.

Vehicle	Estimated initial position $\hat{\mathbf{r}}_0$ [m]						Reference data		
1	-12.72,	0.19,	3.87	(0.03,	0.02,	0.03)	$-$,	$\lvert\cdot\rvert < 4.5$,	$+$
2	12.28,	-0.22,	0.46	(0.03,	0.02,	0.04)	$+$,	$\lvert\cdot\rvert < 4.5$,	$+$
3	-6.49,	-1.09,	0.48	(0.07,	0.04,	0.05)	$-$,	$\lvert\cdot\rvert < 4.5$,	$+$
4	-7.89,	-1.39,	1.02	(0.06,	0.05,	0.05)	$-$,	$\lvert\cdot\rvert < 4.5$,	$+$
5	7.74,	3.91,	3.17	(0.09,	0.08,	0.09)	$+$,	$\lvert\cdot\rvert < 4.5$,	$+$
6	0.36,	*7.76,*	*-1.26*	(0.17,	0.37,	0.15)	$+$,	$\lvert\cdot\rvert < 4.5$,	$+$

Furthermore, the estimated parameters $\mathbf{r}_0$, $\mathbf{v}_0$ and $\mathbf{m}$ can be compared with the available reference data. According to Figure 6.6, Vehicle 1, 3 and 4 are coming from the left and Vehicle 2, 5 and 6 are coming from the right. By consulting the experimental setup in Figure 6.2, this corresponds to a negative and positive x-coordinate for the initial position $\mathbf{r}_0$, respectively. In addition, the y-coordinate is the road center parameter which should be $|\cdot| < 4.5$ since all vehicles pass between the sensors located 4.5 meter from middle of the road. Finally, z-component reveals the height of the car's metallic center above the road plane and should therefore be positive. In Table 6.2 the estimated initial position is given, where also the above discussion of reference data is summarized. Vehicle 1–4 do produce an estimate

that agrees with the reference data, but for Vehicle 5 and 6 this is not the case.

6.4.3 Velocity Estimation

Table 6.3. The estimated velocity $\hat{\mathbf{v}}_0$ in Cartesian coordinates (xyz) for the point target model with standard deviations in parenthesis. Also reference data for the three Cartesian coordinates is given.

Vehicle	Estimated velocity $\hat{\mathbf{v}}_0$ [m/s]						Reference data		
1	5.15,	-0.21,	-0.97	(0.01,	0.01,	0.01)	+,	~ 0,	~ 0
2	-4.91,	0.29,	0.55	(0.01,	0.01,	0.02)	–,	~ 0,	~ 0
3	5.07,	0.15,	0.10	(0.05,	0.03,	0.04)	+,	~ 0,	~ 0
4	4.76,	-0.06,	-0.38	(0.03,	0.03,	0.02)	+,	~ 0,	~ 0
5	-8.66,	*-5.63,*	*-2.47*	(0.08,	0.08,	0.09)	–,	~ 0,	~ 0
6	*0.95,*	*-3.71,*	0.58	(0.23,	0.42,	0.08)	–,	~ 0,	~ 0

In Table 6.3 the estimated velocity is presented together with reference data found in Figure 6.6. Vehicles coming from the left should have a negative velocity in the x-direction and vehicles coming from the right should have a positive velocity in the x-direction. Furthermore, the y- and z-component should be approximately zero in accordance with the experimental setup (see Figure 6.2).

Also here, Vehicles 1–4 do agree with the reference data. However, for Vehicles 5 and 6 it is plausible that the global minimum of the cost function has not been accurately found, which always is a concern then solving non-convex optimization problems. This has probably nothing to do if the vehicle is large or small. Thus, there is no physical explanation why Vehicles 5 and 6 not converge to the correct solution whereas the other vehicles do.

Table 6.4. The estimated magnetic dipole moment $\hat{\mathbf{m}}$ in Cartesian coordinates (xyz) for the point target model with standard deviations in parenthesis.

Veh.	Estimated magnetic dipole moment $\hat{\mathbf{m}}$ [J/T]						$\|\hat{\mathbf{m}}\|$	Rf. data
1	0.387,	-1.244,	-3.483	(0.009,	0.005,	0.009)	3.719	Large
2	0.189,	0.094,	-3.733	(0.017,	0.006,	0.008)	3.739	Large
3	-0.034,	0.031,	-1.224	(0.009,	0.005,	0.016)	1.225	Small
4	-0.340,	-0.205,	-0.853	(0.009,	0.006,	0.016)	0.941	Small
5	0.238,	0.273,	-0.451	(0.006,	0.006,	0.009)	0.579	Small
6	-0.045,	-0.032,	-0.022	(0.015,	0.012,	0.008)	0.059	Small

6.4.4 Dipole Estimation

Furthermore, the magnetic dipole moment is related to the size of the vehicle and its metallic content according to (4.7). Thus, large vehicles should correspond to a large magnetic dipole moment which is verified in Table 6.4.

6.4.5 Magnetic Field Estimation

Finally, by simulating the model with the estimated parameter $\hat{\mathbf{x}}$ we get an estimate of the measured quantity $\hat{\mathbf{y}}_{k,j} = \mathbf{h}_{k,j}(\hat{\mathbf{x}})$, which can be compared with the measured magnetic field $\mathbf{y}_{k,j}$. Note that the residual $\|\mathbf{y}_{k,j} - \hat{\mathbf{y}}_{k,j}\|_{\mathbf{R}_j}$ is exactly what is is being minimized in the NLS framework. In Figure 6.7 the estimated x-component of the magnetic field for sensor 1, $\hat{y}^{(x)}_{1:N,1}$, is compared with its measured equivalence $y^{(x)}_{1:N,1}$. The main character of the signal has been caught. However, there is potential to perform a better fit.

6.5 Extended Target Model Validation

In Section 6.4 the performance of the point target model (4.14) has been analyzed. We have seen that this model did perform well, however not in all aspects satisfactory. In this section the performance of the extended target models described in Section 4.4 will be presented. They are based on the multipole expansion and a row of dipoles, respectively.

6.5.1 Model Order Selection and Model Validation

For the extended target models, an arbitrary model order can be chosen. For the multipole extended target model this model order is the number of multipoles and for the dipole row extended target model it is the number of dipoles. In Figure 6.8 the normalized cost function $V(\hat{\mathbf{x}})/(Nn_y - n_x)$ as a function of model order of these two extended target models is presented.

For all vehicles, the normalized cost function do rapidly decrease with higher model order and the row of dipoles model do generally perform better than the multipole model. For the smaller vehicles it can be seen that the normalized cost function converges towards 1, which corresponds to a correct model.

For the model order $d = 3$ in the row of dipoles model, the equivalent plot to Figure 6.7 can be found in Figure 6.9. From this it can be concluded that an almost optimal fit has been achieved.

This model order will be used for a more thorough analysis. All results for this model order is presented in Table 6.5, 6.6, 6.7 and 6.8 for each vehicle.

In Table 6.5 the normalized cost function for the vehicles is given. We have seen that this quantity should equal one for correct models and by comparing Table 6.5 with Table 6.1 we see that the small vehicles 3–6 have taken huge steps in this direction, whereas the large vehicles 1–2 have a long way to go. This faces the real difficulties finding workable models for large vehicles using models with a reasonable state space dimension.

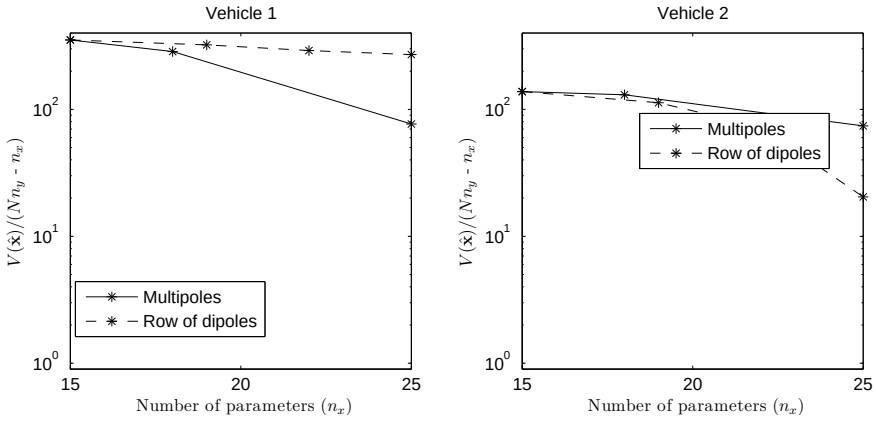

(a) Vehicle 1

(b) Vehicle 2

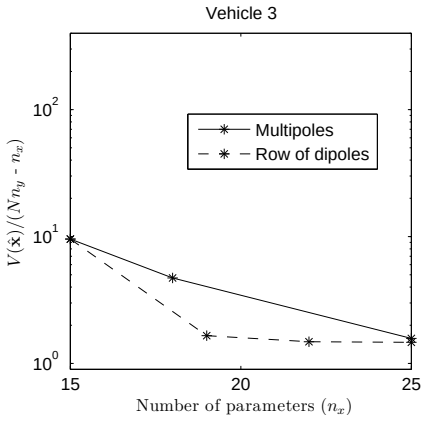

(c) Vehicle 3

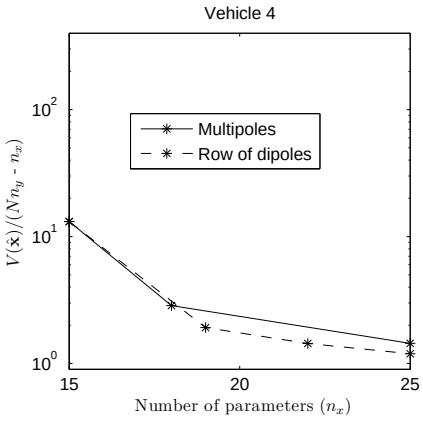

(d) Vehicle 4

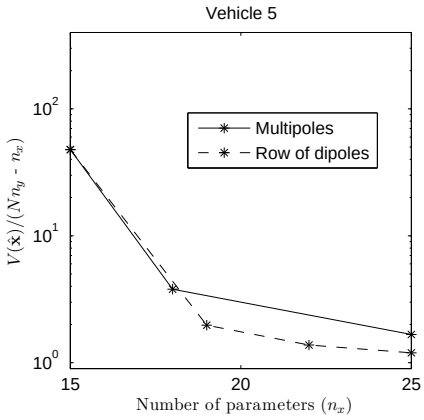

(e) Vehicle 5

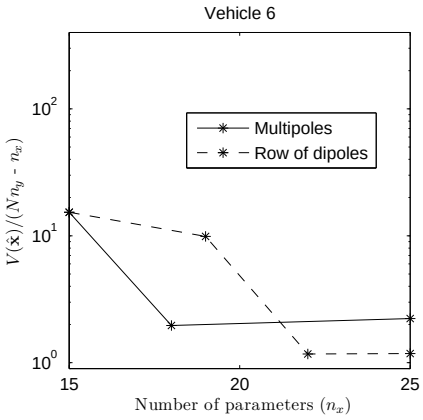

(f) Vehicle 6

Figure 6.8. The normalized cost function $V(\hat{\mathbf{x}})/(Nn_y - n_x)$ as a function of the dimension of the state space (n_x) for multipole extended model up to $p = 3$ multipoles and the row of dipoles extended model up to $d = 4$ dipoles.

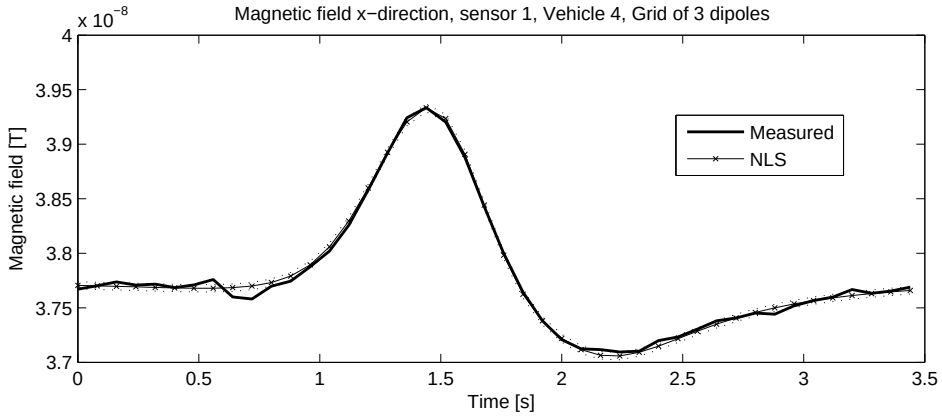

Figure 6.9. The measured magnetic field $y_k^{(x)}$ in the x-direction together with the NLS-estimated value $\tilde{h}_k^{(x)}(\hat{\mathbf{x}})$ for vehicle 4 with a 90 % confidence interval. For the non-linear transformation $\tilde{h}_k^{(x)}(\hat{\mathbf{x}})$ a first order Taylor approximation has been used.

Table 6.5. The normalized cost function for the extended target model $d = 3$.

Vehicle	$V(\hat{\mathbf{x}})/(Nn_y - n_x)$	N	n_y	n_x	Length [m]	
1	302.6	70	6	22	9.09	(0.03)
2	76.7	54	6	22	11.25	(0.04)
3	1.6	32	6	22	3.95	(0.36)
4	1.5	44	6	22	3.56	(0.15)
5	1.5	27	6	22	4.98	(0.25)
6	1.3	22	6	22	2.07	(0.24)

6.5.2 Length Estimation

Extended target models also produce new states, where length of the row of dipoles has a direct physical interpretation. The estimate of this length is also presented in Table 6.5 and do correspond to the size of the vehicles given in Figure 6.6.

6.5.3 Initial state and Velocity Estimation

Furthermore, the extended target model do produce more reasonable estimates of the initial position $\hat{\mathbf{r}}_0$ (see Table 6.6) and the velocity $\hat{\mathbf{v}}_0$ (see Table 6.7) than the point target model did. Now, there are no contradictions between reference data and estimated data. Here, all target trajectories are almost parallel to the x-axis in accordance with the experimental setup and also heading in the correct direction (see Table 6.7).

Table 6.6. The estimated initial position $\hat{\mathbf{r}}_0$ in Cartesian coordinates (xyz) for the extended target model $d = 3$ with standard deviations in parenthesis. Also reference data for the three Cartesian coordinates is given.

Vehicle	Estimated initial position $\hat{\mathbf{r}}_0$ [m]						Reference data		
1	-12.47,	0.13,	4.36	(0.04,	0.02,	0.04)	$-$,	~ 0,	$+$
2	8.64,	-0.13,	1.50	(0.03,	0.02,	0.03)	$+$,	~ 0,	$+$
3	-10.49,	-1.47,	0.57	(0.27,	0.09,	0.09)	$-$,	~ 0,	$+$
4	-8.73,	-2.00,	0.25	(0.14,	0.08,	0.07)	$-$,	~ 0,	$+$
5	11.43,	-1.47,	0.59	(0.20,	0.10,	0.10)	$+$,	~ 0,	$+$
6	8.78,	0.93,	0.42	(0.22,	0.14,	0.09)	$+$,	~ 0,	$+$

Table 6.7. The estimated velocity $\hat{\mathbf{v}}_0$ in Cartesian coordinates (xyz) for the extended target model $d = 3$ with standard deviations in parenthesis. Also reference data for the three Cartesian coordinates is given.

Vehicle	Estimated velocity $\hat{\mathbf{v}}_0$ [m]						Reference data		
1	6.41,	-0.27,	-1.54	(0.02,	0.01,	0.02)	$+$,	~ 0,	~ 0
2	-5.60,	0.33,	0.24	(0.02,	0.01,	0.02)	$-$,	~ 0,	~ 0
3	7.37,	0.33,	0.21	(0.16,	0.06,	0.06)	$+$,	~ 0,	~ 0
4	5.34,	0.28,	0.20	(0.08,	0.05,	0.04)	$+$,	~ 0,	~ 0
5	-9.74,	0.34,	0.02	(0.15,	0.09,	0.08)	$-$,	~ 0,	~ 0
6	-11.56,	1.18,	0.03	(0.25,	0.19,	0.11)	$-$,	~ 0,	~ 0

6.5.4 Height Estimation

Even the z-component of the initial position $\hat{\mathbf{r}}_0$ (see Table 6.6) which corresponds to the height of the car's metallic center over the road plane is more reasonable, being positive for all vehicles and significantly larger for Vehicle 1.

6.5.5 Dipole Estimation

Finally, by making use of the superposition principle (4.16), the total magnetic dipole moment of the vehicles can be found by summarizing all dipoles. This estimate is given in Table 6.8. However, for these values we do not have any reference data more than that large $\hat{\mathbf{m}}$ should correspond to large vehicles. A more thorough analysis of this quantity will be done in the next section by validating (4.7) which relates $\mathbf{m}$ to the vehicle specific parameters, vehicle orientation and the magnetic field of the earth.

Table 6.8. The values of the estimated total magnetic moment $\hat{\mathbf{m}} = \sum_{i=1}^{d} \hat{\mathbf{m}}^i$ in Cartesian coordinates (xyz) for the extended target model $d = 3$ with standard deviations in parenthesis. Also reference data for the three Cartesian coordinates is given.

Vehicle	Estimated magnetic dipole moment $\hat{\mathbf{m}}$ [J/T]						$\|\hat{\mathbf{m}}\|$	Rf. data
1	0.056,	-1.820,	-3.395	(0.022,	0.012,	0.023)	3.853	Large
2	-0.145,	-0.132,	-4.747	(0.044,	0.016,	0.027)	4.751	Large
3	-0.049,	-0.012,	-1.289	(0.018,	0.012,	0.029)	1.290	Small
4	-0.286,	-0.158,	-0.956	(0.018,	0.012,	0.028)	1.010	Small
5	-0.316,	0.315,	-0.973	(0.017,	0.015,	0.029)	1.070	Small
6	0.434,	-0.137,	-0.590	(0.021,	0.016,	0.042)	0.745	Small

6.6 Validation of the Magnetic Dipole Moment

So far the estimated magnetic dipole moment $\hat{\mathbf{m}}$ has only been compared with the size of the vehicle. However, in Chapter 4, $\mathbf{m}$ has been given as a function of vehicle specific parameter, vehicle orientation and the magnetic field of the earth through (4.7). In this section, (4.7) will be validated by estimating $\hat{\mathbf{m}}(\Psi_i)$ for the same vehicle but at different yaw angles Ψ_i relative to the magnetic field of the earth. Hence, throughout this section the coordinate system in Figure 6.10 will be used.

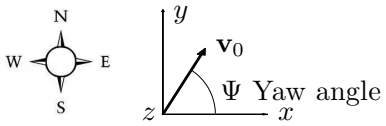

Figure 6.10. The coordinate system used in Section 6.6.

By assuming the pitch angle $\theta = 0°$ this gives

$$\mathbf{m}(\Psi) = \mathbf{R}_z(\Psi)\mathbf{m}_0 + \frac{3D}{\mu_0}\mathbf{B}_0, \tag{6.15}$$

where $\mathbf{R}_z(\Psi)$ is the rotation matrix around the z-axis, $\mathbf{m}_0$ is the permanent magnetic dipole moment of the vehicle, D is a volume characteristic parameter obeying the inequality in (3.37) and $\mathbf{B}_0$ is the magnetic field of the earth.

With the coordinate system in Figure 6.10 we have

$$\mathbf{B}_0 = 1.7 \cdot 10^{-7}[0,\ 0.31,\ -0.95]^T \text{ T},$$

according to our magnetometers. In order to estimate $\hat{\mathbf{m}}(\Psi)$ for different Ψ, Vehicle 5 (see Figure 6.6e) has been used in controlled experiments heading at certain speeds in all four possible directions at the locations given in Figure 6.3 and in Figure 6.11. Thus, measurements for the yaw angles $\Psi = 94.8°,\ 274.8°\ , 29.8°,\ 209.8°$

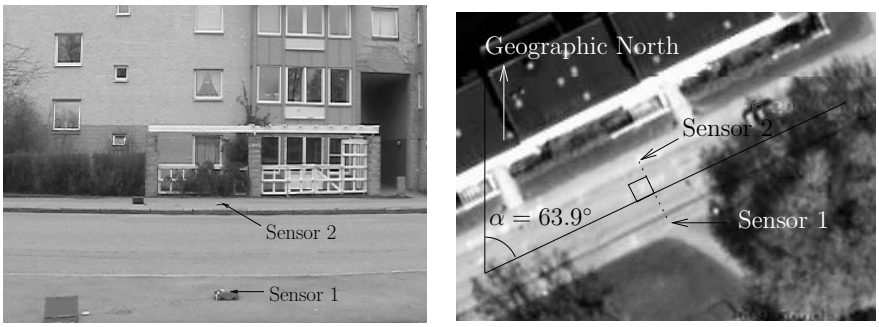

(a) From the side (b) From above

Figure 6.11. The second location used for the validation of (4.7).

have been provided. For each measurement the corresponding $\hat{\mathbf{m}}(\Psi)$ has been estimated with the row of dipoles extended target model, model order $d = 3$, which in Section 6.5 has been proved to be a good model. The results are presented in Table 6.9.

Table 6.9. The true velocity v_0^0 measured with a speedometer and estimated velocity $\hat{v}_0$ and the estimated magnetic dipole moment $\hat{\mathbf{m}}(\Psi)$ for measurements at different yaw angles Ψ.

Ψ	v_0^0	$\hat{v}_0$ [m/s]		Est. magnetic dipole moment $\hat{\mathbf{m}}(\Psi)$ [J/T]					
94.8	5.6	6.12	(0.12)	-0.28,	-0.28,	-0.96	(0.01,	0.01,	0.02)
94.8	11.1	8.40	(0.17)	-0.28,	-0.29,	-0.98	(0.01,	0.02,	0.03)
274.8	8.3	8.57	(0.08)	0.27,	0.67,	-1.06	(0.01,	0.02,	0.03)
274.8	8.3	8.64	(0.07)	0.31,	0.69,	-1.10	(0.01,	0.02,	0.03)
274.8	8.3	8.46	(0.08)	0.25,	0.63,	-1.06	(0.02,	0.02,	0.04)
29.9	2.8	3.94	(0.05)	-0.55,	0.19,	-1.04	(0.01,	0.01,	0.02)
29.9	5.6	6.03	(0.13)	-0.52,	0.12,	-1.04	(0.02,	0.01,	0.02)
29.9	5.6	4.81	(0.11)	-0.50,	0.11,	-1.00	(0.02,	0.01,	0.02)
29.9	2.8	3.49	(0.06)	-0.48,	0.10,	-0.96	(0.02,	0.01,	0.02)
209.9	8.3	8.74	(0.11)	0.59,	0.13,	-1.08	(0.03,	0.01,	0.04)
209.9	8.3	10.00	(0.12)	0.58,	0.14,	-1.02	(0.03,	0.01,	0.05)
209.9	8.3	8.46	(0.09)	0.60,	0.15,	-1.10	(0.03,	0.01,	0.05)
209.9	11.1	11.31	(0.16)	0.60,	0.13,	-1.05	(0.03,	0.02,	0.05)

According to (6.15), $\mathbf{m}(\Psi)$ only depends on the variable Ψ. Thus, $\mathbf{m}(\Psi)$ should be independent of the vehicle speed and from Table 6.9 is can be stated that no such correlation can be found. Furthermore, all $\mathbf{m}(\Psi)$ should be constant for all equal Ψ, which more or less seems to be correct according Table 6.9, however, not with the accuracy that the estimated standard deviations promise. On the other hand, we have seen in Section 6.5 that the row of dipoles model with model order

$d = 3$ does not completely describe the vehicle. Hence, we can not assume $\mathbf{m}(\Psi)$ to be perfectly estimated, however, better than the point target model would do.

Furthermore, since $\mathbf{R}_z(\Psi)$ rotates only around the z-axis, the z-component should be independent of Ψ which also can be verified from Table 6.9. Now we define

$$\mathbf{Y} = \begin{pmatrix} \hat{\mathbf{m}}(\Psi_1) \\ \hat{\mathbf{m}}(\Psi_2) \\ \vdots \\ \hat{\mathbf{m}}(\Psi_i) \\ \vdots \\ \hat{\mathbf{m}}(\Psi_n) \end{pmatrix}, \quad \boldsymbol{\varphi} = \begin{pmatrix} (\mathbf{R}_z(\Psi_1) & 3\mathbf{B}_0/\mu_0) \\ (\mathbf{R}_z(\Psi_2) & 3\mathbf{B}_0/\mu_0) \\ & \vdots \\ (\mathbf{R}_z(\Psi_i) & 3\mathbf{B}_0/\mu_0) \\ & \vdots \\ (\mathbf{R}_z(\Psi_n) & 3\mathbf{B}_0/\mu_0) \end{pmatrix}, \quad \boldsymbol{\theta} = \begin{pmatrix} \mathbf{m}_0 \\ D \end{pmatrix}, \tag{6.16}$$

where i are the different measurements performed at yaw angle Ψ_i. The least squares solution can be found by minimizing the residual $\|\mathbf{Y} - \boldsymbol{\varphi}\boldsymbol{\theta}\|_2$, i.e. by solving

$$(\boldsymbol{\varphi}^T\boldsymbol{\varphi})\boldsymbol{\theta} = \boldsymbol{\varphi}^T\mathbf{Y}$$

The parameter $\boldsymbol{\theta}$ has been estimated to be

$$\hat{\mathbf{m}}_0 = [-0.47,\ 0.29,\ -0.56]^T \text{ J/T}, \qquad \hat{D} = 1.23 \text{ m}^3,$$

which is regarded as a vehicle specific parameter.

Hence, the permanent magnetic dipole moment $\hat{\mathbf{m}}_0$ for Vehicle 5 points back left sloping down relative to the vehicle course (see Figure 6.10 for yaw angle $\Psi = 0$).

The volume characteristic parameter $\hat{D}$ can be compared with the inequality given in (3.37). According to (3.37), $\hat{D}$ should obey

$$V_{fer} < \hat{D} < V,$$

where V_{fer} is the volume of the ferromagnetic steel in the vehicle and V is the volume of the vehicle itself. With a density for steel of 7.8 g/cm^3 we have

$$\text{Volume for Vehicle 5} > 1.23 \text{ m}^3, \tag{6.17a}$$

$$\text{Mass of steel in Vehicle 5} < 1.23 \cdot 7800 = 9600 \text{ kg}, \tag{6.17b}$$

Both of these statements are definitely true for Vehicle 5.

By evaluating (6.15) with $\hat{\mathbf{m}}_0$ and $\hat{D}$ we get an expression $\hat{\hat{\mathbf{m}}}(\Psi)$ for arbitrary Ψ

$$\hat{\hat{\mathbf{m}}}(\Psi) = \mathbf{R}_z(\Psi)\hat{\mathbf{m}}_0 + \frac{3\hat{D}}{\mu_0}\mathbf{B}_0, \tag{6.18}$$

which can be compared with the $\hat{\mathbf{m}}(\Psi)$ given in Table 6.9.

Since the z-component of $\hat{\hat{\mathbf{m}}}(\Psi)$ is independent of Ψ, we have

$$\hat{\hat{m}}^{(z)} = \hat{m}_0^{(z)} + \frac{3\hat{D}B_0^{(z)}}{\mu_0} = -1.04 \text{ J/T}$$

for all Ψ, which agrees with $\hat{m}^{(z)}$ Table 6.9. For the x- and y-component of $\hat{\mathbf{m}}(\Psi)$ and $\hat{\hat{\mathbf{m}}}(\Psi)$ Figure 6.12 illustrates the excellent fit.

By this it can be verified that the magnetic dipole moment $\mathbf{m}$ can be decomposed into two components one being parallel to the magnetic field of the earth with the scalar multiplier $3D/\mu_0$, and one being oriented in the reference frame of the vehicle $\mathbf{m}_0$ where the parameters $\mathbf{m}_0$ and D are vehicle specific. Note that $\mathbf{m}_0$ and D cannot be found only from a single measurement since $\hat{\mathbf{m}}(\Psi)$ contains three components whereas $\mathbf{m}_0$ and D in total contains four.

6.7 Discussion

In this chapter the point and extended target batch models presented in Section 4.3 and 4.4 have been evaluated with real experimental data from various vehicles passing between two magnetometers with constant velocity. The point target model works acceptably for small vehicles and both the multipole extended target model as well as the row of dipole extended target model do significantly improve the data fit. Also the estimated parameters agree with the available reference data. Furthermore, the modeling of the magnetic dipole moment being the sum of two differently oriented components has shown to be correct.

Due to a very good SNR all parameter uncertainties throughout the whole chapter are estimated to be very low. This can for example be seen by comparing the true and estimated velocities in Table 6.9 or by comparing the estimates of the magnetic dipole moments in Figure 6.12 (which all should be equal for the same heading direction). Here, all uncertainties are consequently too small. Thus, we still have model errors with magnitudes nonnegligable to the measurement noise. An even better fit might be achieved with an even higher model order. Also the other possible model errors discussed in Section 4.5 could be considered. This faces the challenging work using signals with very good SNR - very accurate models are needed to extract all possible information!

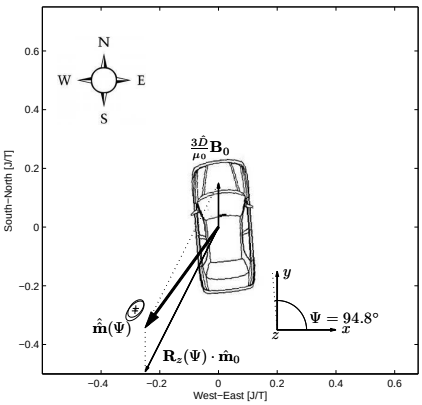

(a) Vehicle 5 heading north on the road in Figure 6.3

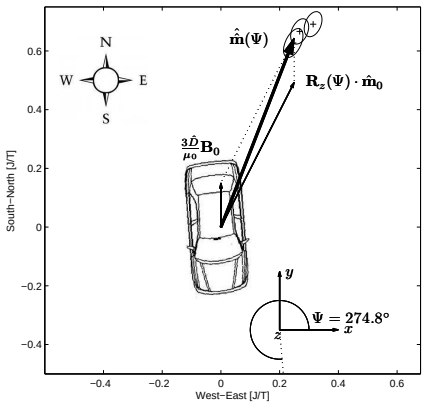

(b) Vehicle 5 heading south on the road in Figure 6.3

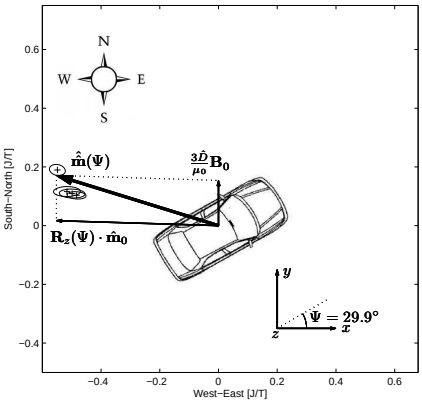

(c) Vehicle 5 heading north east on the road in Figure 6.11

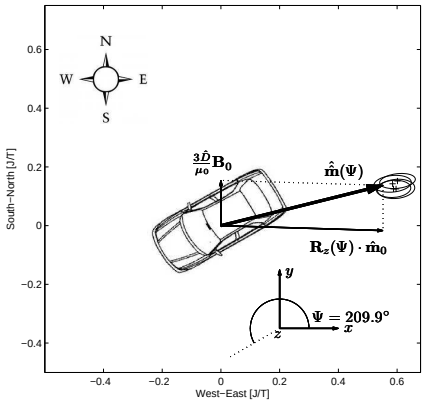

(d) Vehicle 5 heading south west on the road in Figure 6.11

Figure 6.12. The estimated magnetic dipole moment $\hat{\mathbf{m}}(\Psi)$ for different yaw angles Ψ given with a 90% confidence interval (the small ellipses) together with $\hat{\hat{\mathbf{m}}}(\Psi)$ in (6.18). The magnetic dipole moment can successfully be divided into two components, one being parallel to the magnetic field of the earth, and one being oriented in the reference frame of the vehicle.

Chapter 7

Classification and Target Tracking

Two main applications of stationary magnetometers is *classification* and *target tracking*. For automated surveillance systems, vehicle classification can be used for statistical purposes counting specific vehicle models passing a certain intersection. Target tracking information can be used to determine from where to where the vehicles are heading. In this chapter the performance of classification and target tracking will be illustrated with real experimental data.

7.1 Classification

In order to classify vehicles heading in the same direction, their estimated magnetic dipole moment $\hat{\mathbf{m}}$ can be used. For a specific yaw angle Ψ, each vehicle have a characteristic $\mathbf{m}$ given by (4.7). In order to distinguish between two different vehicles, their $\mathbf{m}$ must be separated enough.

In order to examine if two vehicles of similar size could be distinguished, Vehicle 4 (see Figure 6.6d) and Vehicle 5 (see Figure 6.6e) have been used in controlled experiments heading north and south at different speeds at the location given in Figure 6.3. For each scenario, $\hat{\mathbf{m}}$ has been estimated and a projection in the x-y-plane of these estimates is given in Figure 7.1.

Since Vehicle 4 and Vehicle 5 are of equal size, the estimates $\hat{\mathbf{m}}$ are of the same magnitude but are pointing in their own characteristic directions. Hence, there is a great classification potential since the estimates $\hat{\mathbf{m}}$ for the two vehicles are well separated in the x-y-plane.

7.2 Target Tracking

In Chapter 6 only vehicles with constant velocity have been analyzed, i.e. process noise in (4.2) is assumed to be zero. However, in order to track vehicles, one does not want to exclude the possibility to incorporate process noise in the model.

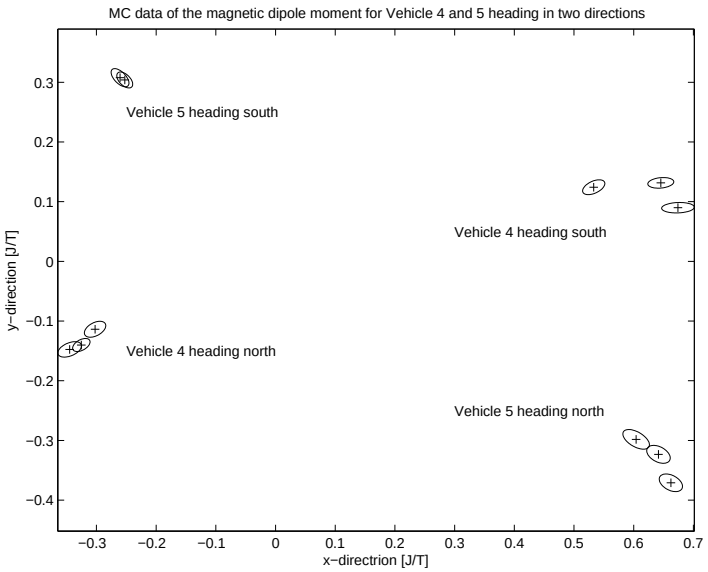

Figure 7.1. The estimated magnetic dipole moment $\hat{\mathbf{m}}$ with a 90% confidence interval (the ellipses) for Vehicle 4 and Vehicle 5 heading north and south at the location given in Figure 6.3. The separation of the estimates indicates great classification potential

Furthermore, in tracking applications the best estimation at each time instance should be provided. Therefore the motion model (4.2) has to be considered. The motion model will be combined with the point target sensor model (4.4) since all extended target models in Section 4.4 are only given in batch formulation, i.e. assuming constant velocity.

In Section 6 we have seen that the point target model does not perform too well if the vehicle is close to the sensor relative to its own characteristic length. By interpreting the point target model as being a truncation of the multipole expansion (3.41) we will get a bias offset defined as the sum of the terms $p = 2, \ldots, \infty$. The magnitude of this bias offset decays as the dominating term $p = 2$ which decays as $\mathcal{O}(\|\mathbf{r}_{k,j}\|^{-4})$ where $\|\mathbf{r}_{k,j}\|$ is the distance from sensor j to the vehicle at time instance $t = kT_s$. This can be used for variance compensation in the EKF by amplifying the measurement noise when the target is close to the sensor. By doing so, we compensate for the unknown bias fault by increasing the covariance matrix. Since the covariance is related to the signal energy of the noise everything has to be squared and we get

$$\mathbf{e}_{k,j} \sim \mathcal{N}\left(\mathbf{0}, \mathbf{R}_j + \left(\frac{\mu_0}{4\pi}\right)^2 \frac{\lambda}{\|\mathbf{r}_{k,j}\|^8} \mathbf{I}_3\right), \tag{7.1}$$

where λ is regarded as a tuning parameter.

Furthermore, the stationary parameter introduced in (4.4), $\mathbf{B}_0$, $\mathbf{m}_0$ and D have to be augmented to the motion model. By assuming no movement in the

z-direction, i.e. $v_k^{(z)} = 0$ and no pitch $\theta = 0$, this results in the following 12-dimensional dynamic state space model

$$r_{k+1}^{(x)} = r_k^{(x)} + T_s v_k^{(x)} + \frac{T_s^2}{2} w_k^{(x)} \tag{7.2a}$$

$$r_{k+1}^{(y)} = r_k^{(y)} + T_s v_k^{(y)} + \frac{T_s^2}{2} w_k^{(y)} \tag{7.2b}$$

$$r_{k+1}^{(z)} = r_k^{(z)} \tag{7.2c}$$

$$v_{k+1}^{(x)} = v_k^{(x)} + T_s w_k^{(x)} \tag{7.2d}$$

$$v_{k+1}^{(y)} = v_k^{(y)} + T_s w_k^{(y)} \tag{7.2e}$$

$$\mathbf{B}_{0,k+1,j} = \mathbf{B}_{0,k,j}, \quad j = 1, 2 \tag{7.2f}$$

$$\mathbf{m}_{0,k+1} = \mathbf{m}_{0,k} \tag{7.2g}$$

$$D_{k+1} = D_k \tag{7.2h}$$

$$\mathbf{y}_{k,j} = \mathbf{B}_{0,k,j} + \frac{\mu_0}{4\pi} \frac{3(\mathbf{r}_{k,j} \cdot \mathbf{m}_k)\mathbf{r}_{k,j} - |\mathbf{r}_{k,j}|^2 \mathbf{m}_k}{|\mathbf{r}_{k,j}|^5} + \mathbf{e}_{k,j}, \quad j = 1, 2 \tag{7.2i}$$

where (7.2j)

$$\mathbf{r}_{k,j} = \mathbf{r}_k - \boldsymbol{\theta}_j \tag{7.2k}$$

$$\mathbf{m}_k = \mathbf{R}_z(\Psi_k)\mathbf{m}_{0,k} + \frac{3D_k}{\mu_0} \frac{\mathbf{B}_{0,k,1} + \mathbf{B}_{0,k,2}}{2}, \tag{7.2l}$$

$$\mathbf{R}_z(\Psi_k) = \begin{pmatrix} \cos\Psi_k & -\sin\Psi_k & 0 \\ \sin\Psi_k & \cos\Psi_k & 0 \\ 0 & 0 & 1 \end{pmatrix}, \quad \Psi_k = \arctan\left(\frac{v_k^{(y)}}{v_k^{(x)}}\right) \tag{7.2m}$$

$$\mathbf{w}_k := [w_k^{(x)},\ w_k^{(y)}]^T \sim \mathcal{N}(\mathbf{0}, \mathbf{Q}), \tag{7.2n}$$

$$\mathbf{e}_{k,j} \sim \left(\mathbf{0}, \mathbf{R}_j + \left(\frac{\mu_0}{4\pi}\right)^2 \frac{\lambda}{\|\mathbf{r}_{k,j}\|^8} \mathbf{I}_3\right). \tag{7.2o}$$

The states $\mathbf{r}_k$, $\mathbf{v}_k$, $\mathbf{B}_{0,k,j}$, $\mathbf{m}_{0,k}$ and D_k, can at each time instant $t = kT_s$ be estimated using the Extended Kalman Filter (see Algorithm 2). $\mathbf{Q}$ and λ are tuning parameters.

To find the initial conditions for the EKF seems to be quite difficult if one does not know anything about the direction from which the vehicle is coming. However, with the prior knowledge that the vehicle follows the roads in a specific intersection, a better prediction of the initial states can be made. In order to track vehicles in the three-way intersection at the location given in Figure 6.3, three EKFs have been initialized, assuming the vehicle is coming from the left, from the right or from the back relative to the camera, respectively. With the filter bank methodology for hypothesis testing described in Section 2.6, the hypotheses $\delta = \{\text{Left}, \text{Right}, \text{Back}\}$ can be defined representing these three differently initialized EKFs. Their probabilities can now be calculated as a function of time. A threshold $\tau = 10^{-12}$ has been chosen to decide when to drop an incorrect hypothesis (see Algorithm 3). The results for three different scenarios is found in Figure 7.2, 7.3

and 7.4 where the tuning

$$\mathbf{Q} = \mathbf{I}_2 \qquad \text{and} \qquad \lambda = 1$$

has been used.

In all three scenarios a correct determination of arrival and heading direction has been accomplished. Furthermore, the limited range of the sensors is illustrated in the trajectories and the filter bank weights. Only when the vehicle is close enough, the correct hypothesis could be found and after the vehicle has passed the sensors, the estimates do not follow the roads in the map, i.e. the sensors have lost the contact with the vehicle.

(a) The vehicle is coming from the left heading right.

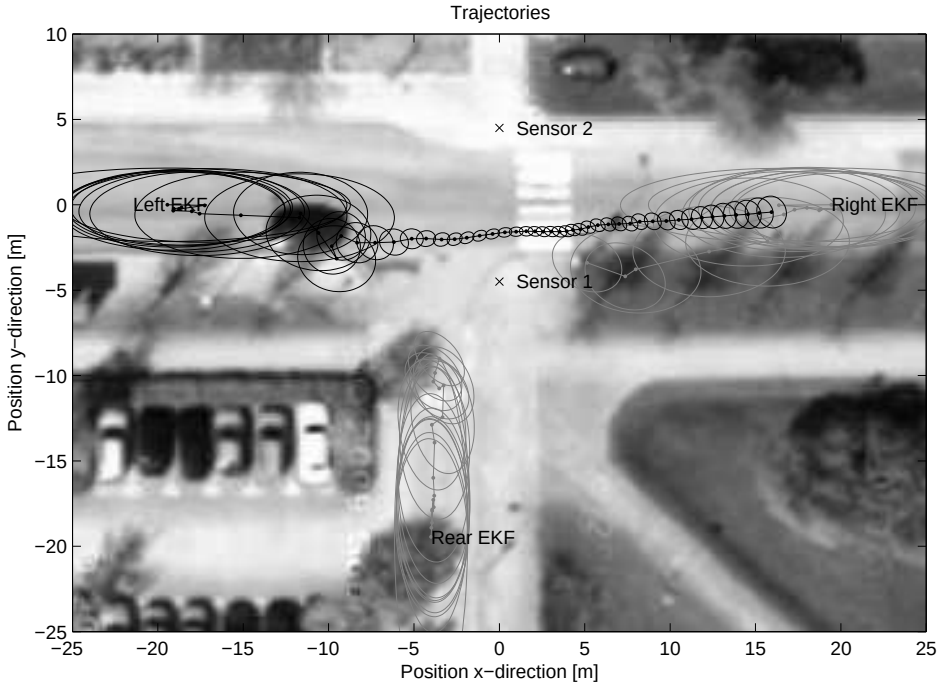

(b) The trajectories according the three different EKFs.

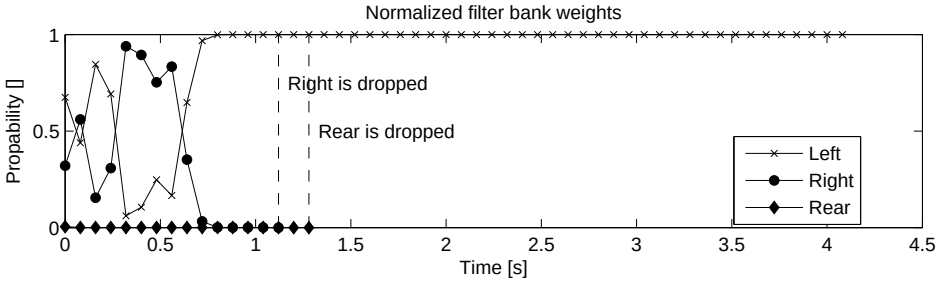

(c) The probabilities $p(\delta{=}\text{Left}|\mathbf{y}_{1:k})$, $p(\delta{=}\text{Right}|\mathbf{y}_{1:k})$ and $p(\delta{=}\text{Rear}|\mathbf{y}_{1:k})$ at time instance $t = kT_s$.

Figure 7.2. Scenario 1. Results from a tracking experiment with three differently initialized EKFs predicting the state of the vehicle in Figure 7.2a presented with a confidence interval of 90%.

(a) The vehicle is coming from the right turning left.

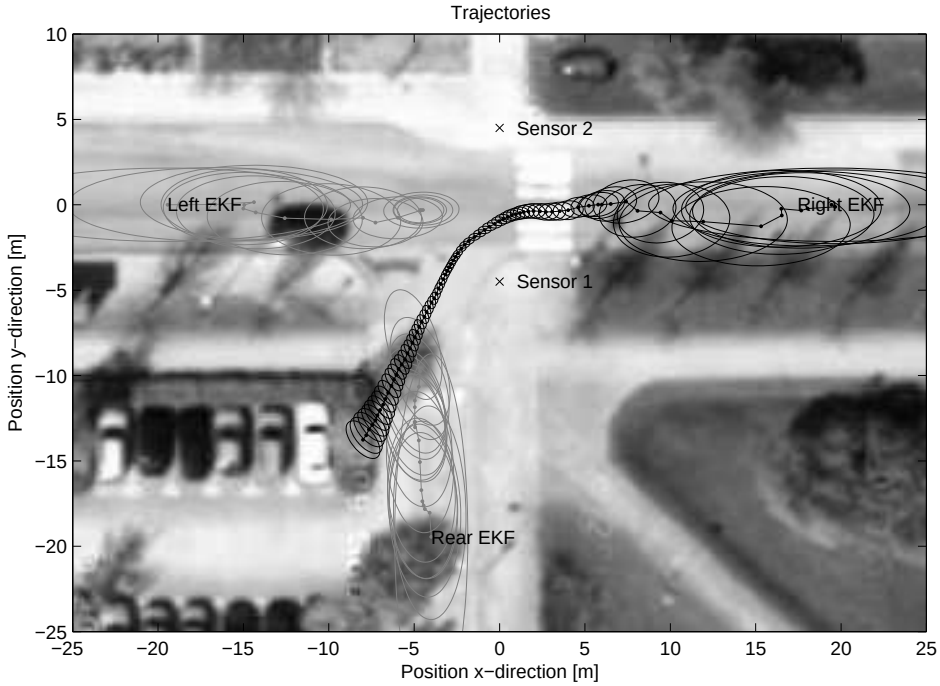

(b) The trajectories according the three different EKFs.

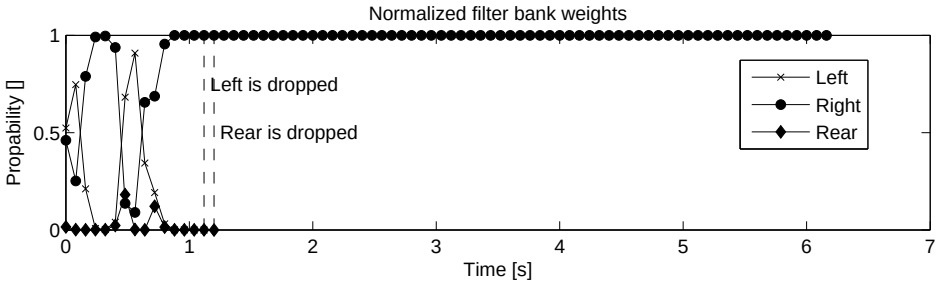

(c) The probabilities $p(\delta{=}\text{Left}|\mathbf{y}_{1:k})$, $p(\delta{=}\text{Right}|\mathbf{y}_{1:k})$ and $p(\delta{=}\text{Rear}|\mathbf{y}_{1:k})$ at time instance $t = kT_s$.

Figure 7.3. Scenario 2. Results from a tracking experiment with three differently initialized EKFs predicting the state of the vehicle in Figure 7.3a presented with a confidence interval of 90%.

(a) The trajectories according the three different EKFs.

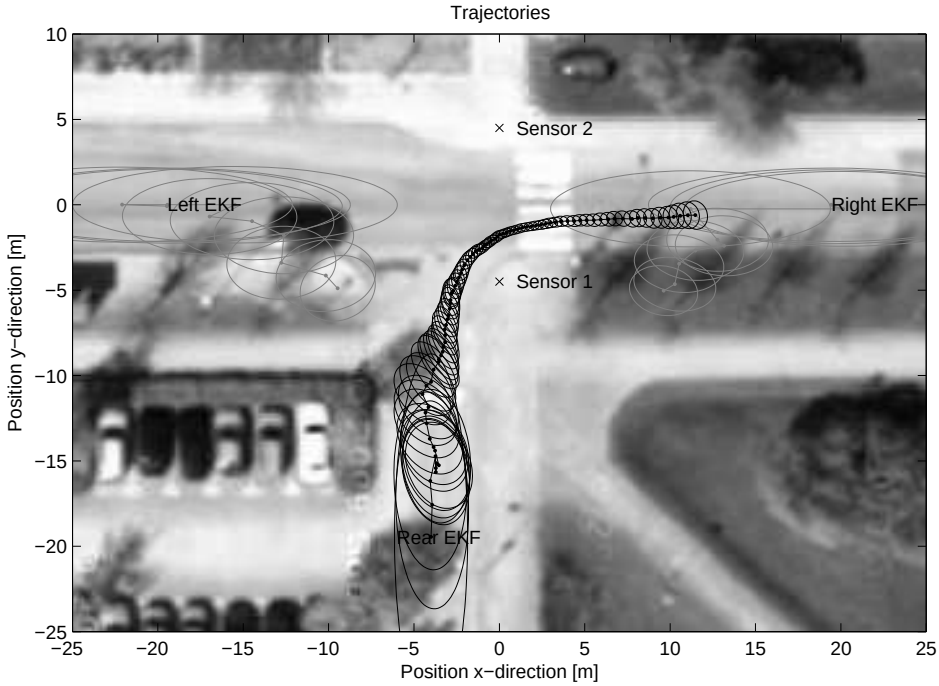

(b) The vehicle is coming from the back turning right.

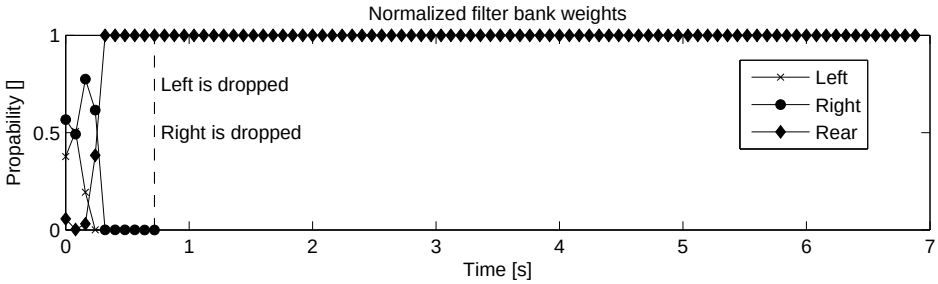

(c) The probabilities $p(\delta{=}\text{Left}|\mathbf{y}_{1:k})$, $p(\delta{=}\text{Right}|\mathbf{y}_{1:k})$ and $p(\delta{=}\text{Rear}|\mathbf{y}_{1:k})$ at time instance $t = kT_s$.

Figure 7.4. Scenario 3. Results from a tracking experiment with three differently initialized EKFs predicting the state of the vehicle in Figure 7.4a presented with a confidence interval of 90%.

Chapter 8

Conclusions and Future Work

The purpose of this thesis was to implement model based signal processing methods for dealing with data from stationary magnetometers measuring the magnetic field of moving vehicles. This implementation has also been evaluated with real experimental data. Furthermore, the theoretical possibilities and limitations of stationary magnetometers for metallic target tracking in general has been analyzed. This chapter discusses the results and presents suggestions for future work in this field.

8.1 Conclusions

It has been found (theoretically and experimentally) that a moving metallic object can be modeled as a magnetic dipole if the distance to the object is large in comparison to its characteristic length. With two magnetometers the position, the velocity and the magnetic dipole moment can be estimated for such objects. A dependency between the magnetic dipole moment and the vehicle orientation has been found making a tracking implementation possible.

Even higher order terms of the model approximation have been analyzed to designing more accurate models, where a row of dipoles significantly could reduce the model error. However, for large vehicles challenging modeling work still remain.

Results from field test data indicate excellent tracking of position and velocity of the target, as well as identification of the magnetic target model suitable for target classification.

The necessity of two magnetometers to uniquely achieve local observability has been stated as well as the optimal sensor deployment of such a two sensor system. Even an effective range of $\sim$ 10 meters for the magnetometer has been found being the main limitation of the sensor in comparison to other sensors common in tracking applications.

8.2 Future work

There is still a lot to be investigated and improved. Here, a few suggestions are presented.

- Finding workable models and signal processing methods for tracking large vehicles.
- Examine the impact and compensate for the other possible model errors presented in Section 4.5, mainly the electromagnetic interaction between the target and other present metallic objects. Maybe a general solution of the magnetostatic equations (3.4) could be considered.
- Analyze the robustness of the methods in more large scale experiments in the order of 10000 vehicles.
- Perform experiments with more accurate reference data.
- The thesis has shown great classification potential for two different vehicles. However, it is still unknown how many vehicles that can be classified.
- The thesis only deals with single target tracking. A future direction could be to investigate multi target tracking.

Bibliography

[1] M. Birsan. Non-linear Kalman filters for tracking a magnetic dipole. In *Proc. of Intl. Conf. on Maritime Electromagnetics, MARELEC*, 2003.

[2] M. Birsan. Unscented particle filter for tracking a magnetic dipole target. In *Proc. of MTS/IEE OCEANS*, 2005.

[3] M. Birsan. Electromagnetic source localization in shallow waters using Bayesian matched-field inversion. *Inverse Problems*, 22(1):43–53, 2006.

[4] J. Callmer, M. Skoglund, and F. Gustafsson. Silent localization of underwater sensors using magnetometers. *Eurasip Journal on Advances in Signal Processing*, 2009.

[5] National Geophysical Data Center. Online declination and field strength calculator. `http://www.ngdc.noaa.gov/geomagmodels/struts/calcIGRFWMM`.

[6] D. K. Cheng. *Field and wave electromagnetics*. Reading, Massachusetts : Addison Wesley, 2 edition, 1989.

[7] Z. A. Daya, D. L. Hutt, and T. C. Richards. Maritime electromagnetism and DRDC signature management research. Technical report, Defence R&D Canada, 2005.

[8] J. Eriksson and M. Varedian. Vägverkets metodbeskrivning för mätning av cykelflöden. Technical report, Vägverket, 2008.

[9] H. González, S. R. Juárez, P. Kielanowski, and M. Loewe. Multipole expansion in magnetostatics. *Am. J. Phys.*, 66, 1998.

[10] F. Gustafsson. *Statistical Sensor Fusion*. Studentlitteratur, 1 edition, 2010.

[11] HyperPhysics. Magnetic properties of ferromagnetic materials. `http://hyperphysics.phy-astr.gsu.edu/Hbase/tables/magprop.html`.

[12] J. D. Jackson. *Classical Electrodynamics*. John Wiley and Sons, Inc., 2 edition, 1975.

[13] J. C. Maxwell. A dynamical theory of the electromagnetic field. *Philosophical Transactions of the Royal Society of London*, 155:459–513, 1865.

[14] D. Törnqvist. Statistical fault detection with applications to IMU disturbances, 2006.

[15] N. Wahlström, J. Callmer, and F. Gustafsson. Magnetometers for tracking metallic targets. In *Proc. of Fusion*, 2010.

[16] Xsens Technologies B.V., http://www.xsens.com. *MTi and MTx User Manual and Technical Documentation*, 2005.

Upphovsrätt

Copyright